A comprehensive framework for high fidelity computations of two-species compressible turbulent flows

Jolan Reynaud, Pierre-Elie Weiss, Sébastien Deck, Philippe Guillen

A comprehensive framework for high fidelity computations of two-species compressible turbulent flows

J.Reynaud[a], P-E.Weiss [1a], S.Deck[a], P. Guillen[a]

[a]*DAAA, ONERA, Université Paris Saclay, F-92190 Meudon, France*

Abstract

A strategy for scale-resolving simulations of bi-species turbulent flows is presented. It relies on a combination of Zonal Detached Eddy Simulation (ZDES) and an original low-dissipative version of the AUSM scheme that adapts its dissipation to capture flow discontinuities while ensuring a low numerical dissipation level in resolved turbulence regions. The corresponding discretized equations are thoroughly detailed. This comprehensive numerical framework is evaluated for the coaxial Air/Argon jet configuration investigated experimentally by Clifton and Cutler [1]. A robust method based on a combination of white noise to generate velocity fluctuations at the inlet of attached turbulent boundary layers together with a dynamic forcing method is applied for the first time in a curvilinear bi-species flow framework with ZDES mode 3. It is shown that the taking into account of resolved turbulence in the incoming attached boundary layers provided by this approach improves the prediction of the mixing process in the early stages of the mixing layer. A good agreement with experiment is also observed with a RANS description of attached boundary layers as permitted by ZDES mode 2 (2020) [2] where the switch between RANS and LES zones is set dynamically by the model itself.

Keywords: ZDES, bi-species flow, turbulent mixing layer, coaxial supersonic jets

1. Introduction

During the ascent of a space launcher, the propulsive jets present supersonic multi-species reactive mixing layers with the external flow. These interactions occurring in the afterbody area of the launcher influence the base drag of the vehicle through a suction effect, the pressure fluctuations levels on the nozzle(s) with noise generation and the base and nozzle(s) temperature due to hot propulsive gas convection [3]. When designing a space launcher, minimizing drag and unsteady loads while providing an optimal thermal protection ensuring the integrity of components with a small amount of added mass constitutes a major challenge [4]. Thus, the study of these mixing layers and the improvement of their numerical characterization [5, 6] is of primary interest for space agencies. The physics of compressible supersonic reactive mixing layers and their numerical modelling have been widely studied for scramjet applications as reviewed in [7]. For these applications, the interactions between fluid dynamics and chemistry are very important in order to control the combustion process. Prior to the consideration of chemistry effects, an important challenge is to perform an accurate

[1]pierre-elie.weiss@onera.fr

modelling of turbulent inert gas mixing [8, 9]. Furthermore, the influence of chemical reactions on space launcher aerodynamics can be small (on base pressure for instance [5]) while the computational cost can increase significantly between an inert and a reactive jet simulation [10].

This article is thus focused on the development of an inert bi-species scale-resolving numerical workflow, intended for space launcher aerodynamics, which aims to simulate the turbulent supersonic mixing of two inert gases. To this end, some issues concerning the modelling of turbulent mass diffusion together with the numerical spatial scheme requirements for supersonic shear flows are first briefly reviewed in the following.

1.1. Review of turbulent mass diffusion modelling techniques

When using a scale separating formulation (RANS, RANS/LES or LES [11]) for a binary gas flow, the influence of unresolved turbulent structures on momentum, energy and mass transport equations has to be modelled. As a turbulent viscosity μ_t is often used for the momentum turbulent diffusion, a common choice in the literature [12, 13] is to define a turbulent Prandtl number Pr_t to evaluate the turbulent heat diffusion coefficient λ_t and a turbulent Schmidt number Sc_t to compute the turbulent mass diffusion coefficient D_t:

$$\lambda_t = \frac{\mu_t c_p}{Pr_t}; \quad D_t = \frac{\mu_t}{\rho Sc_t}. \tag{1}$$

with c_p the constant pressure heat capacity and ρ the fluid density. The idea is to empirically define, thanks to wind-tunnel experiments and advanced numerical simulations, adequate values for these two dimensionless numbers. In practice however, the values for these numbers have been found to vary significantly between flow configurations and even between the different stages of a mixing layer [14, 15]. Several conclusions on the use of these numbers for numerical simulations of supersonic mixing layers are summarized from the literature below.

First, results obtained with RANS computations appear to dramatically depend on the constant values set for turbulent Prandtl and Schmidt numbers [1, 16]. For a defined flow configuration, these values can nevertheless often be adequately tuned *a posteriori* to produce satisfying results [17, 18, 19]. Improved RANS models enabling the spatio-temporal variations of Sc_t and Pr_t have been developed to reduce this sensitivity [8, 9]. However, these models still exhibit case-dependent behaviours and cause an increase of computational costs due to added transport equations. For inert gas mixing simulations, this additional computational cost is not always justified when comparing results with computations using constant Sc_t and Pr_t [20].

RANS/LES computations of supersonic mixing layers have provided results almost independent of the choice of constant values for Sc_t and Pr_t and generally in better agreement with wind tunnel measurements than classical RANS computations [17, 16]. However, with standard RANS/LES formulations, several studies have found an underestimation of turbulent mixing between the two streams, that is to say an undervaluation of the diffusion of the central gas for coaxial configurations [19, 17, 21]. These discrepancies may be attributed to a possible delay in the formation of resolved turbulent structures in the switching area between attached boundary layers treated in RANS and mixing layers treated in LES mode [22]. To overcome this difficulty, some authors have tried to enhance the destruction of the subgrid-scale viscosity by tuning model constants [17] or by using an improved subgrid length-scale [19], both studies report a noticeable overestimation of

turbulent mixing with those solutions. The introduction of turbulent content in the attached boundary layers is then mentioned as a possible solution to reproduce a realistic turbulent mixing between the two flows. Such a method has been used in [21]. However, these authors also report a strong overestimation of turbulent mixing which is attributed to the settings of turbulence generation and to the use of a too dissipative numerical scheme. Another attempt to improve RANS/LES prediction for supersonic coaxial jet was proposed in [23] with the use of a variable Sc_t/Pr_t model. Such an approach led to an overestimation of turbulent mixing for locations after 10 center jet diameters.

1.2. Numerical strategy for RANS/LES computations of supersonic bi-species mixing layers

The choice of the numerical methods has a dramatic influence on the accuracy of RANS/LES computations of supersonic bi-species mixing layers. Two main opposite issues have to be dealt with. On the one hand, the numerical dissipation of the methods has to be as low as possible in order to enable the onset of resolved turbulent content in the early stages of the mixing layer [24], to resolve accurately the large turbulent eddies driving the mixing between the two fluids [25] and to properly convect the turbulent structures from the attached boundary layers when they are resolved. Among others, Simon et al. [24] have shown that the dissipation level of the spatial numerical scheme influences the size of the resolved turbulent scales and the time averaged properties of an axisymmetric mixing layer. On the other hand, as shock structures arise from the interaction between the two supersonic flows, the numerical methods have to be robust enough near these structures in order to capture discontinuities without triggering numerical instabilities [26].

In order to contribute to the development of advanced numerical methods for bi-species supersonic mixing layers, two bi-species ZDES [22] computations are performed in this study on a well-known supersonic coaxial jets experiment run by Cutler et al. [27, 1] and reproduced numerically by several authors in the past with RANS [1, 18] or RANS/LES formulations [17, 23, 19, 21]. To meet the numerical challenges described above, the computations are run with an original hybrid numerical scheme [28] based on Ducros's sensor [29] associated to a low dissipation version of the AUSM scheme [30, 31]. This new scheme is able to switch automatically from a low-dissipation formulation in presence of vortical structures to a more robust formulation in presence of shock waves (see Sec.3.1). The two present calculations differ by the treatment of the attached boundary layers which are either treated with a URANS mode or with a Wall-Modelled Large Eddy Simulation (WMLES) mode by taking into account turbulent fluctuations in the incoming attached boundary layers. The separated mixing layers are simulated in LES mode for both calculations. These approaches are briefly discussed in Sec.2.3. The present computations are performed thanks to the extension of the FLU3M solver [32] from mono-species to bi-species ZDES computations. The developments needed for such an extension are detailed in Sec.3.

1.3. Organization of the paper

The paper is organized as follows: The salient features of the physical modelling of the bi-species framework for compressible turbulent flows are firstly reminded in Section 2. The discretized form of these models is then thoroughly detailed in Section 3. Further practical details regarding the numerical implementation

of the implicit convective and diffusive fluxes are provided in appendices A and B. The test case and the meshing strategy are presented in Section 4 and this new framework is finally exercised and compared with the experiments and numerical computations published in the literature in Section 5.

2. Governing equations

To describe an inert bi-species perfect gas flow, one can use the general conservative form of scale separated (averaged or filtered) Navier-Stokes equations:

$$\frac{\partial \mathbf{w}_c}{\partial t} + div(\mathcal{F}) = div(\mathcal{G}) \tag{2}$$

$\mathbf{w}_c =^t (\rho_1, \rho_2, \rho\mathbf{V}, \rho E)$ denotes the vector of conserved quantities, containing 6 variables against 5 in a mono-species case. ρ_1 et ρ_2 are the two gases densities and ρ is the density of the mixture. $\mathbf{V} =^t (u, v, w)$ is the velocity vector of the flow and E represents the mixture total energy. $\mathcal{F}$ and $\mathcal{G}$ are the convection and diffusion terms:

$$\mathcal{F} =^t (\rho_1\mathbf{V}, \rho_2\mathbf{V}, \rho\mathbf{V}\otimes\mathbf{V} + P\overline{\overline{I}}, (\rho E + P)\mathbf{V}) \tag{3}$$

$$\mathcal{G} =^t (\mathbf{J}_1^*, \mathbf{J}_2^*, \overline{\overline{\tau^*}}, \overline{\overline{\tau^*}}.\mathbf{V} - \mathbf{q}^* - \mathbf{J}_E^*) \tag{4}$$

With P the mixture pressure, $\mathbf{J}_i^* = \mathbf{J}_i + \mathbf{J}_{t_i}$ the total mass flux of the ith species with $\mathbf{J}_i$ the laminar mass flux and $\mathbf{J}_{t_i}$ the unresolved turbulent mass flux , $\mathbf{q}^* = \mathbf{q} + \mathbf{q}_t$ the total heat flux with $\mathbf{q}$ the laminar heat flux and $\mathbf{q}_t$ the unresolved turbulent heat flux, $\mathbf{J}_E^*$ the total energy flux. $\overline{\overline{\tau^*}}$ is the combination of the viscous stress and the unresolved turbulent stress tensors:

$$\tau_{ij}^* = 2(\mu + \mu_t)(S_{ij} - \frac{1}{3}\delta_{ij}S_{ii}) \qquad i,j = 1..3 \tag{5}$$

$$S_{ij} = \frac{1}{2}(\frac{\partial u_i}{\partial x_j} + \frac{\partial u_j}{\partial x_i}) \qquad i,j = 1..3 \tag{6}$$

with μ being the molecular viscosity and μ_t being the turbulent eddy (resp. subgrid scale) viscosity which is provided by the underlying RANS (resp. subgrid scale) model.

2.1. Thermodynamic Properties

Several equations describing the thermodynamic properties of the two calorically perfect gases and the transport properties of the flow are needed to close the governing equations. First, the density of the mixture is defined as:

$$\rho = \rho_1 + \rho_2 = \rho(Y_1 + Y_2) \tag{7}$$

with Y_i the mass fraction of the ith species. As a consequence of this definition, one can note that:

$$Y_1 + Y_2 = 1 \quad \text{and} \quad \nabla Y_1 = -\nabla Y_2 \tag{8}$$

The thermodynamic properties for each of the two gases (i=1,2) are defined as:

$$\gamma_i = \frac{c_{p_i}}{c_{v_i}}, \quad c_{p_i} - c_{v_i} = r_i \tag{9}$$

c_{p_i} et c_{v_i} being the constant pressure and the constant volume heat capacities, γ_i the specific heat ratio and r_i the specific gas constant. Supposing a thermal equilibrium between the two gases, the internal energy e_i and the specific enthalpy h_i are defined as:

$$e_i = c_{v_i} T \quad , \quad h_i = c_{p_i} T = \gamma_i e_i = e_i + \frac{P_i}{\rho_i} \tag{10}$$

Those quantities being extensive properties, one deduces:

$$\rho e = \rho_1 e_1 + \rho_2 e_2 = \rho(Y_1 c_{v_1} + Y_2 c_{v_2}) T \tag{11}$$

$$\rho h = \rho_1 h_1 + \rho_2 h_2 = \rho(Y_1 c_{p_1} + Y_2 c_{p_2}) T \tag{12}$$

Thus, for the mixture, one can define:

$$c_v = Y_1 c_{v_1} + Y_2 c_{v_2}, \quad c_p = Y_1 c_{p_1} + Y_2 c_{p_2} \tag{13}$$

$$\gamma = \frac{c_p}{c_v} = \frac{Y_1 \gamma_1 c_{v_1} + Y_2 \gamma_2 c_{v_2}}{Y_1 c_{v_1} + Y_2 c_{v_2}}, \quad r = c_p - c_v = Y_1 r_1 + Y_2 r_2 \tag{14}$$

Then, using Dalton's Law for calorically perfect gas, we obtain the mixture pressure as the sum of both partial pressures and the equation of state for the mixture. We finally relate the internal energy to the pressure and express the mixture total energy.

$$P = P_1 + P_2 = (\rho_1 r_1 + \rho_2 r_2) T = \rho r T \tag{15}$$

$$P = \rho r \frac{e}{c_v} = \rho(\gamma - 1) e, \quad \rho E = \rho e + \frac{1}{2}\rho \mathbf{V}^2, \quad \rho H = \rho h + \frac{1}{2}\rho \mathbf{V}^2 \tag{16}$$

With H being the total enthalpy of the mixture. Assuming Eq. 17, the hyperbolicity of the implicit system is preserved. Indeed, the Jacobian matrix of the convective fluxes displayed in appendix A (see Eq. A.1) can be diagonalized with the eigenvalues $(\mathbf{V}.\mathbf{n} - a, \mathbf{V}.\mathbf{n} + a, \mathbf{V}.\mathbf{n})$, the latter being quadrupled. This ensures the hyperbolicity of the convective set of equations (see Abgrall [33]) and enables to define the mixture speed of sound (with frozen gas composition):

$$a^2 = \frac{\gamma P}{\rho} \tag{17}$$

2.2. Transport Properties

2.2.1. Viscous Fluxes

An acknowledged approximation for binary gas mixture is to define the viscosity as a weighted sum of the two species viscosity [13]:

$$\mu = Y_1 \mu_1 + Y_2 \mu_2 \tag{18}$$

For each species, the molecular viscosity μ_i is given by a Sutherland's law:

$$\mu_i(T) = \mu_{0_i} \left(\frac{T}{T_{0_i}} \right)^{\frac{3}{2}} \frac{T_{0_i} + S_i}{T + S_i} \tag{19}$$

The total viscosity can thus be defined as $\mu^* = \mu + \mu_t$.

2.2.2. Energy Flux

The heat flux $\mathbf{q}$ is given by Fourier's law:

$$\mathbf{q} = -\lambda \nabla T \tag{20}$$

A thermal conductivity is defined for each species thanks to a constant Prandtl number Pr_i and the thermal conductivity of the mixture is then estimated as a viscosity-weighted average of both conductivities [13]:

$$\lambda_i = \frac{\mu_i c_{p_i}}{Pr_i}, \quad \lambda = \mu(\frac{\lambda_1}{\mu_1} Y_1 + \frac{\lambda_2}{\mu_2} Y_2) \tag{21}$$

To account for the effect of unresolved turbulence on heat transfer, the unresolved turbulent heat flux $\mathbf{q}_t$ is modelled thanks to a turbulent Prandtl number defined for the mixture flow:

$$\mathbf{q}_t = -\lambda_t \nabla T, \quad \lambda_t = \frac{\mu_t c_p}{Pr_t} \tag{22}$$

The total thermal conductivity is then defined as $\lambda^* = \lambda + \lambda_t$. In a mixture, the energy flux is moreover related to the diffusion of enthalpy:

$$\mathbf{J}_E^* = \mathbf{J}_1^* h_1 + \mathbf{J}_2^* h_2 \tag{23}$$

2.2.3. Mass Diffusion

To model laminar mass diffusion fluxes, the Hirschfelder-Curtis approximation [34] is considered as the most accurate first-order approximation available. For a binary gas mixture, it resumes to Fick's diffusion law [35]:

$$\mathbf{J}_1 = -\rho D \nabla Y_1, \quad \mathbf{J}_2 = -\rho D \nabla Y_2 \tag{24}$$

where $D = \mathcal{D}_{12} = \mathcal{D}_{21}$ denotes the mixture diffusion coefficient. This formulation traduces the tendency to balance mass fractions as the fluxes are opposed to mass fraction gradients. The mass conservation condition can be verified:

$$\mathbf{J}_1 + \mathbf{J}_2 = -\rho D(\nabla Y_1 + \nabla Y_2) = 0 \tag{25}$$

The diffusion coefficient D may be derived from particle collision models and thermodynamic variables, it is known to vary as $D \sim \frac{T^{3/2}}{P}$ [36]. For fluid mechanics problems with inert gases, a simplified model is usually chosen. D is defined thanks to the Schmidt Number Sc expressing a ratio between viscous and mass diffusions:

$$D = \frac{\mu}{\rho Sc} \tag{26}$$

A common hypothesis, with good experimental support [37, 38], is to consider Sc constant for a pair of gases. As for heat transfer, a turbulent diffusion coefficient is furthermore defined to compute $\mathbf{J}_{t_i} = -\rho D_t \nabla Y_i$ the

unresolved turbulent mass fluxes. This coefficient is expressed thanks to a turbulent Schmidt number to form the total diffusion coefficient:

$$D_t = \frac{\mu_t}{\rho Sc_t}, \quad D^* = D + D_t \tag{27}$$

As explained in Sec.1.1, Sc and Sc_t are usually defined empirically with wind tunnel experiments and numerical simulations.

2.3. Turbulence modelling using Zonal Detached Eddy Simulation (ZDES)

ZDES is a multiresolution approach developed by ONERA [22, 39] which aims at treating in a single model all classes of flow problems indicated in Fig 1. In this approach, three specific hybrid length scale formulations (see Eq.(28)) also called modes are optimized to be used on three typical flowfield topologies as illustrated in Fig 1. In the frame of the Spalart-Allmaras model [40], $\tilde{d}_{ZDES}$ replaces the distance to the wall d_w according to:

$$\tilde{d}_{ZDES} = \tilde{d}_{mode}\left(\tilde{\Delta}, d_w, U_{i,j}, \nu, \tilde{\nu}, \frac{\partial\tilde{\nu}}{\partial n}, \frac{\partial||\boldsymbol{\omega}||}{\partial n}\right) \tag{28}$$

$$mode = 1, 2, 3 \tag{29}$$

with $\tilde{\Delta}$ denoting the subgrid length scale entering $\tilde{d}_{ZDES}$ that depends on the grid cell size, $U_{i,j}$ the velocity gradients, d_w the distance to the wall, $||\boldsymbol{\omega}||$ the magnitude of vorticity, ν and $\tilde{\nu}$ the kinematic and pseudo eddy viscosity as well as $\frac{\partial\tilde{\nu}}{\partial n}$ the derivative in the wall-normal direction. The definition of $\tilde{d}_{ZDES}$ is not a minor adjustment in the DES framework since the modified lengthscales depend not only on the grid but also on the velocity and eddy viscosity fields and their wall-normal derivatives. ZDES takes full advantages of its zonal nature since complex configurations can be accurately treated by the use of various fomulations within the same calculation (an example is provided in [41]).

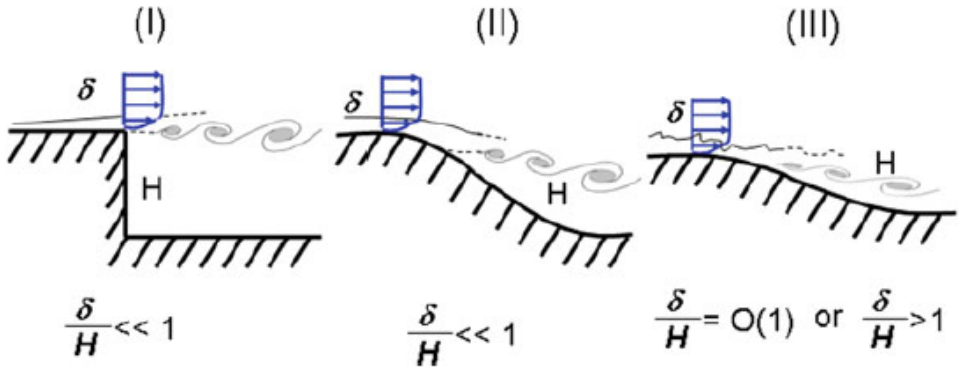

Figure 1: Classification of typical flow problems. I: separation fixed by the geometry, II: separation induced by a pressure gradient on a curved surface, III: separation strongly influenced by the dynamics of the incoming boundary layer

In this study, we have first computed a bi-species turbulent mixing case with the recent version of the ZDES Mode 2 (2020) [2] (computation ZDES C1) to assess the newly developed bi-species numerical framework in comparison with experimental measurements and previous RANS/LES computations from the literature.

This mode of the ZDES approach is designed to treat attached boundary layers in RANS mode and to automatically switch to a LES mode to treat detached flows.

Then, to evaluate the influence of turbulent content coming from the attached boundary layer on the mixing process and to demonstrate the abilities of the ZDES, the framework of the ZDES Mode 3 [42, 43] has been used to provide stimulated boundary layers (SBL) referred to as (ZDES C2). With ZDES mode 3, the inner part of the boundary layer is treated with RANS equations and the outer part is treated in LES mode. The separation between both parts is given by a RANS/LES interface defined by the user as a fraction of the RANS boundary layer thickness, typically $d_w^{interface} = 0.125\delta(x)$. Example of WMLES (Wall Modelled LES) use of ZDES are given in [42, 44]. A more detailed description of the boundary layer treatments applied is given in Sec.4.2.

3. Numerical Methods

The FLU3M solver [45] developed by ONERA is used to solve the compressible Navier-Stokes equations on multiblock structured grids. An implicit finite volume form of the governing equations (Eq.(2)), based on Gear's second-order accurate time discretization, yields for a hexahedral cell centered in (i,j,k) with a volume Ω_{ijk}:

$$\begin{aligned}\frac{3}{2}\Delta\left(\mathbf{w}_c\right)_{ijk}^{n+1,p+1} + \frac{\Delta t}{\Omega_{ijk}}\sum_{l=1}^{6}\left[\left(\frac{\partial \mathbf{F}(\mathbf{w}_c)}{\partial \mathbf{w}_c} - \frac{\partial \mathbf{G}(\mathbf{w}_c)}{\partial \mathbf{w}_c}\right)_{ijk,l}^{n+1,p}\Delta(\mathbf{w}_c)_{ijk}^{n+1,p+1}\right] = \\ \frac{3}{2}(\mathbf{w}_c)_{ijk}^{n} - \frac{3}{2}(\mathbf{w}_c)_{ijk}^{n+1,p} + \frac{1}{2}\Delta\left(\mathbf{w}_c\right)_{ijk}^{n} - \frac{\Delta t}{\Omega_{ijk}}\sum_{l=1}^{6}\left(\mathbf{F}(\mathbf{w}_c) - \mathbf{G}(\mathbf{w}_c)\right)_{ijk,l}^{n+1,p}\end{aligned} \tag{30}$$

Where p is the index of inner iteration, n and $n+1$ represent consecutive iterations in time and $\Delta\left(\mathbf{w}_c\right)_{ijk}^{n+1} = (\mathbf{w}_c)_{ijk}^{n+1} - (\mathbf{w}_c)_{ijk}^{n}$. The inner iterations are used to ensure the Newton convergence process $(\mathbf{w}_c)^{n+1,p+1} - (\mathbf{w}_c)^{n+1,p} = \Delta\left(\mathbf{w}_c\right)^{n+1,p+1} \rightarrow 0$ leading to $(\mathbf{w}_c)^{n+1} = (\mathbf{w}_c)^{n+1,p+1} \approx (\mathbf{w}_c)^{n+1,p}$ for the last inner iteration for which Eq. 30 becomes:

$$\begin{aligned}\frac{3}{2}\Delta\left(\mathbf{w}_c\right)_{ijk}^{n+1} - \frac{1}{2}\Delta\left(\mathbf{w}_c\right)_{ijk}^{n} + \frac{\Delta t}{\Omega_{ijk}}\sum_{l=1}^{6}\left(\mathbf{F}(\mathbf{w}_c) - \mathbf{G}(\mathbf{w}_c)\right)_{ijk,l}^{n} = \\ -\frac{\Delta t}{\Omega_{ijk}}\sum_{l=1}^{6}\left[\left(\frac{\partial \mathbf{F}(\mathbf{w}_c)}{\partial \mathbf{w}_c} - \frac{\partial \mathbf{G}(\mathbf{w}_c)}{\partial \mathbf{w}_c}\right)_{ijk,l}^{n}\Delta(\mathbf{w}_c)_{ijk}^{n+1}\right]\end{aligned} \tag{31}$$

For each interface l associated to a normal vector $\mathbf{n}=^t (n_x, n_y, n_z)$ and a surface $\Delta S_{ijk,l}$, the discrete convective and diffusive fluxes $\mathbf{F}$ and $\mathbf{G}$ are defined as:

$$\mathbf{F}(\mathbf{w}_c)_{ijk,l} = \begin{pmatrix}\rho_1(\mathbf{V}.\mathbf{n}) \\ \rho_2(\mathbf{V}.\mathbf{n}) \\ \rho u(\mathbf{V}.\mathbf{n}) + Pn_x \\ \rho v(\mathbf{V}.\mathbf{n}) + Pn_y \\ \rho w(\mathbf{V}.\mathbf{n}) + Pn_z \\ (\rho E + P)(\mathbf{V}.\mathbf{n})\end{pmatrix}_{ijk,l} .\Delta S_{ijk,l} \tag{32}$$

$$\mathbf{G}(\mathbf{w}_c)_{ijk,l} = \begin{pmatrix} \mathbf{J}_1^*.\mathbf{n} \\ \mathbf{J}_2^*.\mathbf{n} \\ \tau_{xx}^* n_x + \tau_{xy}^* n_y + \tau_{xz}^* n_z \\ \tau_{xy}^* n_x + \tau_{yy}^* n_y + \tau_{yz}^* n_z \\ \tau_{xz}^* n_x + \tau_{yz}^* n_y + \tau_{zz}^* n_z \\ (\overline{\overline{\tau}}^*.\mathbf{V} - \mathbf{q}^* + \mathbf{J}_E^*).\mathbf{n} \end{pmatrix}_{ijk,l} .\Delta S_{ijk,l} \tag{33}$$

Based on previous works [33, 32], several numerical methods of the FLU3M solver have been enhanced in order to achieve RANS and ZDES implicit computations of viscous and turbulent bi-species flows. These adaptations concern numerical methods designed for convective fluxes (Sec. 3.1), explicit diffusion fluxes (Sec. 3.2), implicit treatment (Sec. 3.3), boundary conditions treatment (Sec. 3.4), dynamic forcing (Sec. 3.5) and post-processing methods (not detailed here, see [16]).

3.1. Explicit convective fluxes

In order to test different numerical strategies, we have adapted three mono-species schemes to bi-species flow: the AUSM+ [30], a robust upwind scheme, an adapted low-dissipative AUSM+(P) [31] (called here AUSM+(P) L-D) and a hybrid shock-capturing scheme combining the two previous AUSM type schemes to perform high-fidelity, scale-resolving simulations of compressible flows [28].

3.1.1. AUSM+ 2S

The AUSM+ scheme has been proposed by Liou [30] for a mono-species flow, an adaptation to binary gas mixture (AUSM+ 2S) is presented here. The main idea here is to decompose the non-viscous fluxes $\mathbf{F}(\mathbf{w}_c)$ between convective fluxes $\mathbf{F}^{(c)}$ and acoustic fluxes $\mathbf{P}$.

$$\mathbf{F}(\mathbf{w}_c) = \mathbf{F}^{(c)} + \mathbf{P} \tag{34}$$

For a bi-species flow, these fluxes can be written as:

$$\mathbf{F}^{(c)} = Ma.^t(\rho_1, \rho_2, \rho\mathbf{V}, \rho H), \quad \mathbf{P} =^t (0, 0, Pn_x, Pn_y, Pn_z, 0) \tag{35}$$

assuming M=$\frac{\mathbf{V}.\mathbf{n}}{a}$, a the speed of sound and H the total enthalpy, $H = E + \frac{P}{\rho}$.
For the sake of explanation, suppose that we are willing to compute this AUSM+ (AU) flux $\boldsymbol{F}_{j+\frac{1}{2}}^{AU}$ through the interface between the cell *(i,j,k)* and the cell *(i,j+1,k)*. We need to express a convective numerical flux $\mathbf{f}_{j+1/2}^{(c)}$ and a pressure numerical flux $\mathbf{p}_{j+1/2}$. Defining $a_{j+1/2}$ as the cell interface speed of sound one can write:

$$\mathbf{f}_{j+1/2}^{(c)} = m_{j+1/2} a_{j+1/2} \boldsymbol{\Psi}_{j+1/2}, \quad \boldsymbol{\Psi} =^t (\rho_1, \rho_2, \rho\mathbf{V}, \rho H) \tag{36}$$

and

$$\mathbf{p}_{j+1/2} =^t (0, 0, Pn_x, Pn_y, Pn_z, 0)_{j+1/2} \tag{37}$$

$\boldsymbol{\Psi}_{j+1/2}$ is given by a basic upwinding procedure:

$$\boldsymbol{\Psi}_{j+1/2} = \begin{cases} \boldsymbol{\Psi}_L & if \quad m_{j+1/2} \geq 0 \\ \boldsymbol{\Psi}_R & otherwise \end{cases} \tag{38}$$

With $\Psi_{L,R}$ being the left and right states obtained for the interface $j+\frac{1}{2}$ with the chosen MUSCL reconstruction. The terms $m_{j+1/2}$, $\boldsymbol{p}_{j+1/2}$ and $a_{j+1/2}$ have yet to be defined. Liou [30] proposes a decomposition of those terms as the sum of two contributions:

$$m_{j+1/2} = \mathcal{M}^{+}(M_j) + \mathcal{M}^{-}(M_{j+1}) \tag{39}$$

$$\boldsymbol{p}_{j+1/2} = \mathcal{P}^{+}(M_j)\boldsymbol{p}_j + \mathcal{P}^{-}(M_{j+1})\boldsymbol{p}_{j+1} \tag{40}$$

with:

$$\mathcal{M}^{\pm}(M) = \begin{cases} \dfrac{1}{2}(M \pm |M|), & if \quad |M| \geq 1 \\ \pm\dfrac{1}{2}(M \pm 1)^2 \pm \dfrac{1}{8}(M^2-1)^2 & otherwise \end{cases} \tag{41}$$

$$\mathcal{P}^{\pm}(M) = \begin{cases} \dfrac{1}{2}(1 \pm sign(M)), & if \quad |M| \geq 1 \\ \pm\dfrac{1}{4}(M \pm 1)^2(2 \pm M)^2 \pm \dfrac{3}{16}M(M^2-1)^2 & otherwise \end{cases} \tag{42}$$

For the common speed of sound, a simple arithmetic average at the interface yields satisfying results:

$$a_{j+1/2} = \frac{1}{2}(a_j + a_{j+1}) \tag{43}$$

The adaptation to binary gas mixture mostly consists in the definition of $\boldsymbol{\Psi}$ and in the use of local mass fractions for the computation of thermodynamic variables at the center of cells $(a_j, \boldsymbol{p}_j)$ as in equations (7),(14), (15) and (17). The AUSM+ 2S numerical flux $\boldsymbol{F}^{AU}_{j+\frac{1}{2}}$ is finally computed as:

$$\boldsymbol{F}^{AU}_{j+\frac{1}{2}} = m_{j+1/2}a_{j+1/2}\boldsymbol{\Psi}_{j+1/2} + \boldsymbol{p}_{j+1/2} \tag{44}$$

This scheme is known for its good shock-capturing properties but is too dissipative for high-fidelity scale-resolving simulations [46].

3.1.2. AUSM+(P) L-D

Mary and Sagaut [31] proposed a simplified formulation of the AUSM+(P) scheme designed to ensure a low numerical dissipation for scale-resolving simulations. We recall here the main features of this scheme and the adjustments needed for binary mixture flow. The Euler fluxes are approximated by:

$$\boldsymbol{F}^{LD}_{j+\frac{1}{2}} = V_1\frac{\Psi_L + \Psi_R}{2} - |U_{dis}|\frac{\Psi_R - \Psi_L}{2} + P_1 \tag{45}$$

With V_1 the interface fluid velocity, P_1=$[0, 0, \frac{P_L+P_R}{2}n_x, \frac{P_L+P_R}{2}n_y, \frac{P_L+P_R}{2}n_z, 0]$ and $\Psi_{L,R}$ being the left and right states obtained with the chosen MUSCL reconstruction. U_{dis} is a parameter based on the local fluid velocity to control the numerical dissipation. More precisely, V_1 is computed with a pressure stabilization term:

$$V_1 = \frac{(\boldsymbol{V}_L + \boldsymbol{V}_R).\boldsymbol{n}}{2} - c_2(P_R - P_L) \tag{46}$$

U_{dis} is defined as:

$$U_{dis} = \zeta * max(|\frac{(\boldsymbol{V}_L + \boldsymbol{V}_R).\boldsymbol{n}}{2}|, c_1) \tag{47}$$

c_1 and c_2 are constant parameters based on the flow reference values ($c_1 = 0.04 * U_\infty$ and $c_2 = 0.04 * \frac{1}{U_\infty \rho_\infty}$) and $\zeta \in \{0; 1\}$ is a sensor used to minimize dissipation by enabling a fully centered scheme in monovariant zones [31]. The adaptation to binary gas mixture here again stands in the definition of $\Psi =^t (\rho_1, \rho_2, \rho\mathbf{V}, \rho H)$ and the computation of thermodynamic quantities.

The sensor formulation ζ is adapted from [31] to be active on six equations rather than five for the mono-species. To detect spurious oscillations at the interface $j + \frac{1}{2}$, the definition of ζ is based on two functions, Δ_ξ^j to detect changes in the sign of the slopes of a variable ξ and $W_{w_{p_k}}$ applied on primitive variables $\mathbf{w}_p =^T (\rho_1, \rho_2, \mathbf{V}, P)$ to detect consecutive sign changes corresponding to oscillations:

$$\Delta_\xi^j = \begin{cases} -1 \quad if \quad (\xi_{j+2} - \xi_{j+1})(\xi_{j+1} - \xi_j) < 0 \\ \qquad\qquad 1 \quad otherwise \end{cases} \tag{48}$$

$$W_{w_{p_k}} = \begin{cases} 1 \quad if \quad \Delta_{w_{p_k}}^j + \Delta_{w_{p_k}}^{j+1} < 0 \quad or \quad \Delta_{w_{p_k}}^j + \Delta_{w_{p_k}}^{j-1} < 0 \\ \qquad\qquad 0 \quad otherwise \end{cases} \tag{49}$$

$$\zeta = max[(W_{w_{p_k}})_{k=1..6}] \tag{50}$$

This scheme has been used with success on various configurations for scale-resolving computations ([47, 48, 49, 50, 51] among others), but is not adapted for flow configurations leading to the formation of shock waves.

3.1.3. Hybrid shock-capturing scheme

Based on the two numerical schemes presented above, a hybrid scheme has been recently proposed in [28]. This scheme blends the two previously described formulations to ensure both a low numerical dissipation and good local shock-capturing properties. The chosen formulation is:

$$\boldsymbol{F}_{j+\frac{1}{2}} = \boldsymbol{F}_{j+\frac{1}{2}}^{LD} + \beta \boldsymbol{F}_{j+\frac{1}{2}}^{AU} \tag{51}$$

With β a sensor designed to detect shocks, based on Ducros's [29] sensor Φ:

$$\Phi = \frac{(\nabla.\mathbf{u})^2}{(\nabla.\mathbf{u})^2 + (\boldsymbol{\nabla} \wedge \mathbf{u})^2 + \epsilon} \quad \epsilon = 1.10^{-32} s^{-2} \tag{52}$$

$\nabla.\mathbf{u}$ is the divergence of the velocity vector, it takes high values near shocks and $\nabla \wedge \mathbf{u}$ evaluates the vorticity of the flow, it takes high values in vortical regions. Thus, $\Phi \in [0; 1]$ and it takes values close to one near a shock wave and close to zero in vortical regions. A more complete formulation has been derived to enhance dissipation near shocks, to maintain β between 0 and 1 and to ensure a smooth variation of β limiting sensitivity to numerical wiggles:

$$\beta(\Phi) = tanh(3 * \Phi) \tag{53}$$

The spatial accuracy of the present schemes is finally extended thanks to the MUSCL approach. A second-order Minmod MUSCL reconstruction [52] is employed with the AUSM+ scheme for the internal flows and a third-order Koren-type MUSCL reconstruction [53] is used with the hybrid scheme to treat the mixing and the stimulated boundary layers. See [28] for more details on these MUSCL procedures as the adaptation to

bi-species flows only consists in the straightforward extension of these procedures to six equations instead of five.

3.2. Explicit Diffusive fluxes

To assess the diffusion flux vector $\mathbf{G}$ (see Eq.33), values of $\rho, D^*, \mu^*, \lambda^*, \mathbf{V}, h_i$ at the cell interface are needed. They are estimated by taking the average of the center values in the right and left cells. Estimations of velocity, mass fraction and temperature gradients are also required. To this end, a corrected Green-Gauss mono-species approach described in [54] is adapted to include mass fraction gradient computations. It is designed to prevent numerical instabilities that can arise due to odd-even decoupling oscillations allowed by the original Green-Gauss approach.

3.3. Implicit fluxes

As seen in equation (31), Jacobian matrices of the fluxes are needed for the implicit formulation of the time scheme:

$$A = \left(\frac{\partial \mathbf{F}}{\partial \mathbf{w}_c}\right)^n_{ijk,l}, \quad B = \left(\frac{\partial \mathbf{G}}{\partial \mathbf{w}_c}\right)^n_{ijk,l} \tag{54}$$

To compute A and B at a cell interface, the procedure exposed in [55] has been adapted. A convenient first step is to express the matrix $M^{-1} = (\frac{\partial \mathbf{w}_p}{\partial \mathbf{w}_c})$ transforming partial derivatives with respect to the primitive variables $\mathbf{w}_p =^T (\rho_1, \rho_2, \mathbf{V}, P)$ into partial derivatives with respect to conservative ones and its inverse $M = (\frac{\partial \mathbf{w}_c}{\partial \mathbf{w}_p})$. In particular, for a bi-species flow, variations of P with respect to ρ_1 and ρ_2 require some developments. From (15) and (14) we write:

$$P = \frac{Y_1 c_{v_1}(\gamma_1 - 1) + Y_2 c_{v_2}(\gamma_2 - 1)}{Y_1 c_{v_1} + Y_2 c_{v_2}} (\rho E - \frac{1}{2}\frac{\rho^2 \mathbf{V}^2}{\rho_1 + \rho_2}) \tag{55}$$

Assuming:

$$X = \frac{P c_{v_1} c_{v_2}(\gamma_1 - \gamma_2)}{(\rho_1 c_{v_1} + \rho_2 c_{v_2})(\rho_1 r_1 + \rho_2 r_2)} \tag{56}$$

One can show that:

$$\frac{\partial P}{\partial \rho_1} = \rho_2 X + \frac{1}{2}(\gamma - 1)\mathbf{V}^2, \quad \frac{\partial P}{\partial \rho_2} = -\rho_1 X + \frac{1}{2}(\gamma - 1)\mathbf{V}^2 \tag{57}$$

The matrix M^{-1} can then be expressed as:

$$M^{-1} = \begin{pmatrix} 1 & 0 & 0 & 0 & 0 & 0 \\ 0 & 1 & 0 & 0 & 0 & 0 \\ -\frac{u}{\rho} & -\frac{u}{\rho} & \frac{1}{\rho} & 0 & 0 & 0 \\ -\frac{v}{\rho} & -\frac{v}{\rho} & 0 & \frac{1}{\rho} & 0 & 0 \\ -\frac{w}{\rho} & -\frac{w}{\rho} & 0 & 0 & \frac{1}{\rho} & 0 \\ \rho_2 X + \frac{1}{2}(\gamma - 1)\mathbf{V}^2 & -\rho_1 X + \frac{1}{2}(\gamma - 1)\mathbf{V}^2 & -(\gamma - 1)u & -(\gamma - 1)v & -(\gamma - 1)w & \gamma - 1 \end{pmatrix} \tag{58}$$

And M is then found as:

$$M = \begin{pmatrix} 1 & 0 & 0 & 0 & 0 & 0 \\ 0 & 1 & 0 & 0 & 0 & 0 \\ u & u & \rho & 0 & 0 & 0 \\ v & v & 0 & \rho & 0 & 0 \\ w & w & 0 & 0 & \rho & 0 \\ \frac{\frac{1}{2}(\gamma-1)\mathbf{U}^2 - \rho_2 X}{\gamma - 1} & \frac{\frac{1}{2}(\gamma-1)\mathbf{U}^2 + \rho_1 X}{\gamma - 1} & \rho u & \rho v & \rho w & \frac{1}{\gamma - 1} \end{pmatrix} \tag{59}$$

3.3.1. Convective flux

After re-writing the convective fluxes with the explicit appearance of the conservative variables:

$$\mathbf{F}(\mathbf{w}_c) = \begin{pmatrix} \rho_1 \mathbf{V}.\mathbf{n} \\ \rho_2 \mathbf{V}.\mathbf{n} \\ \rho u \mathbf{V}.\mathbf{n} + P n_x \\ \rho v \mathbf{V}.\mathbf{n} + P n_y \\ \rho w \mathbf{V}.\mathbf{n} + P n_z \\ (\rho E + P)\mathbf{V}.\mathbf{n} \end{pmatrix} .\Delta S_{ijk,l} = \begin{pmatrix} \frac{\rho_1}{\rho_1+\rho_2}\rho \mathbf{V}.\mathbf{n} \\ \frac{\rho_2}{\rho_1+\rho_2}\rho \mathbf{V}.\mathbf{n} \\ \frac{\rho u}{\rho_1+\rho_2}\rho \mathbf{V}.\mathbf{n} + P n_x \\ \frac{\rho v}{\rho_1+\rho_2}\rho \mathbf{V}.\mathbf{n} + P n_y \\ \frac{\rho w}{\rho_1+\rho_2}\rho \mathbf{V}.\mathbf{n} + P n_z \\ \frac{(\rho E+P)}{\rho_1+\rho_2}\rho \mathbf{V}.\mathbf{n} \end{pmatrix} .\Delta S_{ijk,l} \tag{60}$$

One can use M^{-1} to derive the Jacobian matrix A with respect to the conservative variables (shown in Tab.A.4 in Appendix A).

3.3.2. Viscous Fluxes

For the implicit part of the viscous fluxes, a five-step procedure is applied to approximate the contribution of the Jacobian matrix of $\mathbf{G}$. Only the last step corresponds to a program implemented in the solver. These steps are listed here but the details of the operations are displayed in Appendix B:

1. Express explicitly the viscous flux vector $\mathbf{G}$ (B.1) and detail the spatial derivatives contained in this vector with respect to primitive variables.
2. Compute the matrix $(\frac{\partial \mathbf{G}}{\partial \mathbf{w}_{p_a}})_{ijk,l}$ for $a = x, y, z$. The example for $a = x$ is given in (B.6)
3. Compute the Jacobian matrix $(\frac{\partial \mathbf{G}}{\partial \mathbf{w}_p})_{ijk,l}$ thanks to the approximation:

$$(\frac{\partial \mathbf{G}}{\partial \mathbf{w}_p})_{ijk,l} = \left(\sum_{a \in (x,y,z)} (\frac{\partial \mathbf{G}}{\partial \mathbf{w}_{p_a}}).\frac{\partial \eta}{\partial a} \right)_{ijk,l} \tag{61}$$

   With η being the normal component in a local frame linked the cell interface l (B.8) and using the approximation $(\frac{\partial \eta}{\partial a})_{ijk,l} = \frac{S_a}{\Omega}$ with S_a the surface normal to the a direction, Ω the volume of the cell and $S = S_x^2 + S_y^2 + S_z^2$.
4. Compute the Jacobian matrix of $\mathbf{G}$ with respect to conservative variables (B.7):

$$(\frac{\partial \mathbf{G}}{\partial \mathbf{w}_c})_{ijk,l} = (\frac{\partial \mathbf{G}}{\partial \mathbf{w}_p} M^{-1})_{ijk,l} \tag{62}$$

5. Use Coakley's method [56] to estimate the contribution of this matrix by the maximum of its eigenvalues $B \approx (\delta.\frac{S^2}{\Omega})_{ijk,l}.I_6$ with:

$$\delta_{ijk,l} = max(D^*, \frac{4}{3}\nu^*, \frac{\lambda^*}{\rho c_v})_{ijk,l} \tag{63}$$

The 6×6 matrix (instead of 5×5 for a mono-species flow) obtained for the left term of Eq.31 will finally be inverted thanks to a lower-upper (LU) resolution algorithm [57].

While the discretization of the explicit part of the Navier-Stokes conservative variables consists in a second order scheme through the MUSCL approach, the treatment of the explicit part of the $\rho\tilde{\nu}$ equation is based on a first order upwind scheme. The implicit step is based on a LU-SGS algorithm is thus decoupled between the conservative variables and the turbulent one ([58, 59]).

3.4. Boundary conditions

In the FLU3M solver, the boundary conditions are treated with ghost cells [57] (cell 0 in Fig.2) placed at the frontier of the domain and parametrized to compute adequate fluxes at the interface with the frontier (cell 1 on Fig.2).

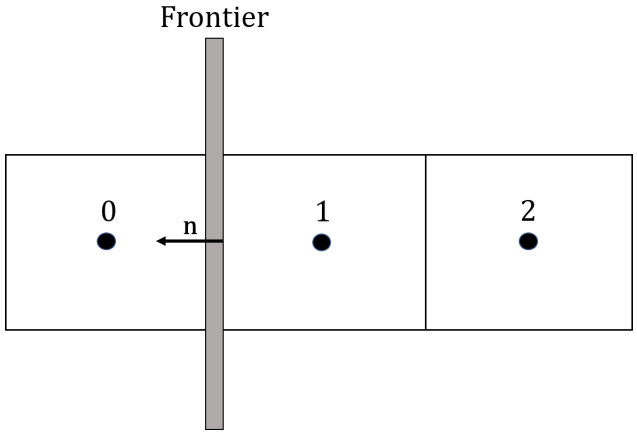

Figure 2: Schematic of a ghost cell approach. Here $\mathbf{n}$ is the external normal vector for cell 1

3.4.1. Adiabatic wall

To simulate an adiabatic wall in a mono-species computation (5 equations), one has to ensure several conditions at the interface between the fluid and the wall, that is to say at the interface between the frontier cell and the ghost cell:

- the no-slip condition $\mathbf{V} =^t (u, v, w) = (0, 0, 0)$
- a null normal pressure gradient $\frac{\partial P}{\partial \mathbf{n}} = 0$
- a null normal thermal gradient $\frac{\partial T}{\partial \mathbf{n}} = 0$

This is done by setting $\mathbf{V}_0 = -\mathbf{V}_1$, $P_0 = P_1$ and $e_0 = e_1$. The adaptation to bi-species flow (6 equations) lies in the computation of the mixture pressure P and the mixture internal energy e thanks to relations described in Sec.2.1 and in the addition of a null normal mass fraction condition $\frac{\partial Y_i}{\partial \mathbf{n}} = 0$ ensured by forcing $Y_{1_0} = Y_{1_1}$ which implies $Y_{2_0} = Y_{2_1}$ according to Eq.8.

3.4.2. Free surface

As described in [55], free surface boundary conditions are treated using the resolution of a linearized Riemann problem. Indeed, neglecting viscous terms and using the hypothesis of a one-dimensional flow in the direction normal to the interface ($\mathbf{n}$) one can linearise Eq.2 in the form:

$$\frac{\partial \mathbf{w}_c}{\partial t} + A\frac{\partial \mathbf{w}_c}{\partial n} = 0 \tag{64}$$

An efficient way of computing the solution is to rewrite Eq.64 using the primitive variables $\mathbf{w}_p$ thanks to the previously defined matrices $M^{-1} = (\frac{\partial \mathbf{w}_p}{\partial \mathbf{w}_c})$ and $M = (\frac{\partial \mathbf{w}_c}{\partial \mathbf{w}_p})$, one can thus obtain:

$$\frac{\partial \mathbf{w}_p}{\partial t} + \underbrace{M^{-1}AM}_{J} \frac{\partial \mathbf{w}_p}{\partial n} = 0 \tag{65}$$

With J the Jacobian matrix of the convective fluxes with respect to the primitive variables detailed in the Appendix A.5. One can see that this matrix has the form $J = (\mathbf{V}.\mathbf{n}) \times I_6 + J_0$ where J_0 does not depend on speed components. The left and right eigenvectors of J can thus also be chosen as independent of $\mathbf{V}.\mathbf{n}$. The matrices of the right eigenvectors R and left eigenvectors L (With $LR = I_6$) can be expressed as:

$$R = \begin{pmatrix} 1 & 0 & 0 & 0 & \frac{\rho_1}{a} & \frac{\rho_1}{a} \\ 0 & 1 & 0 & 0 & \frac{\rho_2}{a} & \frac{\rho_2}{a} \\ 0 & 0 & \left(\frac{n_z n_x}{N_{xy}} \quad or \quad n_z\right) & \left(\frac{-n_y}{N_{xy}} \quad or \quad 0\right) & n_x & -n_x \\ 0 & 0 & \left(\frac{n_z n_y}{N_{xy}} \quad or \quad 0\right) & \left(\frac{n_x}{N_{xy}} \quad or \quad 1\right) & n_y & -n_y \\ 0 & 0 & -N_{xy} & 0 & n_z & -n_z \\ 0 & 0 & 0 & 0 & \rho a & \rho a \end{pmatrix} \tag{66}$$

$$L = \begin{pmatrix} 1 & 0 & 0 & 0 & 0 & \frac{-\rho_1}{a^2} \\ 0 & 1 & 0 & 0 & 0 & \frac{-\rho_2}{a^2} \\ 0 & 0 & \left(\frac{n_z n_x}{N_{xy}} \quad or \quad n_z\right) & \left(\frac{n_z n_y}{N_{xy}} \quad or \quad 0\right) & -S_{xy} & 0 \\ 0 & 0 & \left(\frac{-n_y}{N_{xy}} \quad or \quad 0\right) & \left(\frac{n_x}{N_{xy}} \quad or \quad 1\right) & 0 & 0 \\ 0 & 0 & \frac{1}{2}n_x & \frac{1}{2}n_y & \frac{1}{2}n_z & \frac{1}{2\rho a} \\ 0 & 0 & -\frac{1}{2}n_x & -\frac{1}{2}n_y & -\frac{1}{2}n_z & \frac{1}{2\rho a} \end{pmatrix} \tag{67}$$

With $N_{xy} = \sqrt{n_x^2 + n_y^2}$ when $\frac{1}{N_{xy}}$ is defined and $N_{xy} = n_z, 0$ or 1 otherwise. For R, the first two columns correspond to the species transport with the eigenvalues $\alpha_1 = \alpha_2 = \mathbf{V}.\mathbf{n}$, the next two to the transport of the interface speed components normal to $\mathbf{n}$, with the eigenvalue $\alpha_3 = \alpha_4 = \mathbf{V}.\mathbf{n}$, and the two last columns corresponds quantities transported by the acoustic eigenvalues $\alpha_5 = \mathbf{V}.\mathbf{n} + a$ and $\alpha_6 = \mathbf{V}.\mathbf{n} - a$. The left eigenvector matrix L has a strictly similar structure by lines. One can see that the extension to multispecies flow is straightforward.

Defining the Jacobian matrix J for the average state $\mathbf{w}_{c_{avg}} = \frac{\mathbf{w}_{c_0} + \mathbf{w}_{c_1}}{2}$ to evaluate the matrix L and the eigenvalues α_i at the cell interface, the left (0) and right (1) states at the frontier can be projected on the eigenvector basis to form characteristic variables: $\omega = L\mathbf{w}_p$. Eq.65 then becomes:

$$\frac{\partial \boldsymbol{\omega}_i}{\partial t} + \alpha_i \frac{\partial \boldsymbol{\omega}_i}{\partial \mathbf{n}} = 0 \quad i = 1...6 \tag{68}$$

The characteristic state at the interface $0, 1$ between the ghost cell and the frontier cell are then chosen as:

$$\boldsymbol{\omega_i}_{0,1} = \begin{cases} \boldsymbol{\omega_i}_1 & if \quad \alpha_i > 0 \\ \boldsymbol{\omega_i}_0 & otherwise \end{cases} \tag{69}$$

The flux corresponding to the state $(\mathbf{w}_p)_{0,1} = R\boldsymbol{\omega}_{0,1}$ obtained with the chosen characteristics variables are then computed at the interface according to Eq.32. This way, any subsonic or supersonic entrance/exit can be treated in a non-reflexive way with a correct input of information.

3.4.3. User's input

In the bi-species numerical framework implemented, the user has to define Sutherland's laws constants (see Eq.19) [μ_{0_i},S_i,T_{0_i}] and [γ_i, c_{v_i}, Pr_i] for the two gases (i=1,2) involved in the simulation and [Pr_t, Sc, Sc_t] for the mixture. These quantities enable to initialize the conservative variables ($\rho_1 = \rho * Y_1, \rho_2 = \rho * Y_2, \rho\mathbf{V}, \rho E$) and the transport coefficients in any zone of the computational domain.

3.5. Dynamic forcing

As explained in Sec.2.3, the ZDES mode 3 framework is built to treat the outer part of a boundary layer in LES mode. As discussed by Laraufie et al.[46], such framework has to be fed with turbulent content. In this study, we chose to use the method described in [60] that is based on a physics motivated combination of white noise to generate fluctuations at the inlet of the boundary layer domain together with a dynamic forcing method processing the inlet velocity fluctuations. The dynamic forcing, based on the idea proposed by Spille-Kohoff and Kaltenbach [61], consists in the addition of a source-term to the momentum equations in order to increase the resolved turbulent kinetic energy. This source term is built as a closed-loop controller adjusting the velocity components to match the target wall-normal Reynolds stress levels prescribed by a previously performed RANS computation of the current configuration. As for the adaptation of numerical schemes to bi-species flow, the modification of dynamic forcing consists in the use of the mixture properties to compute the source term.

4. Test case

The test case is based on the coaxial jet experiment presented by Cutler and coworkers in [27, 1] which was designed for CFD code validation. A summary of previous computational studies of this case found in the literature is presented in Table 1. In the version studied here, two co-flowing supersonic jets of argon (center jet) and air (outer jet) discharge in a quiescent atmosphere. The short review (see Table 1) reveals that only few hybrid RANS/LES approaches with stimulated incoming boundary layers have been used to study this case.

4.1. Experimental setup

The axisymmetric geometry of the coaxial jet experiment by Clifton and Cutler is shown in Fig.3 (dimensions provided in mm). It consists of a center body and a concentric outer body. The center body contains a supersonic nozzle for the argon jet with an exit diameter D_{cj}=10 mm and the gap between the center and outer bodies creates a supersonic nozzle for the coflow air jet with an exit outer diameter D_{coflow}=60.47 mm. The two nozzles were designed to provide a nominal Mach number of 1.8 at the exit. This corresponds to a velocity $U_i = 400 \quad m/s$ ($Re_{D_{cj}} = 1.3.10^5$) for the inner argon jet and a velocity $U_o = 480 \quad m/s$

Study	Center jet gas	Turbulence modelling	S_{c_t}	N_{xyz}	$\Delta\theta$
Clifton and Cutler (2007) [1]	Ar and He-O_2	RANS $k-\omega$	0.1/0.25/0.5/0.9	$0.19.10^6$	2D-axi
Baurle et al. (2010) [17]	Ar and He-O_2	RANS/LES	0.25/0.5/1	43.10^6	-
Cocks et al. (2012) [21]	He-O_2	SST DDES + SBL	0.5/1	22.10^6	-
Dharavath et al. (2015)[18]	Ar and He-O_2	RANS $k-\epsilon$	constant	$0.45.10^6$	0.8° on a 10° angular slice
Charrier et al. (2016) [23]	He-O_2	DDES ($k-\epsilon$)	variable	14.10^6	1.5°
Troshin et al. (2019) [19]	Ar and He-O_2	SST DDES	constant	10.10^6	-
Reynaud et al. (2020) [16]	Ar	RANS S-A and ZDES	0.25/0.5/1	65.10^6	1.8°
Present study	Ar	ZDES Mode 2 + SBL	0.5	165.10^6	1°

Table 1: Overview of numerical studies of the supersonic coxial experiments of Cutler et al. [27, 1]. SBL: Stimulated Boundary Layers.

($Re_{D_{coflow}} = 4.8.10^5$) for the outer air jet and thus to a velocity ratio $r_u = \frac{U_o}{U_i} = 1.2$. The jets discharge in a cylindrical plenum (40 cm diameter and 110 cm length) filled with air at atmospheric pressure. The initial flow conditions in terms of total pressure (P_{tot}) and total temperature (T_{tot}), including the coflow jet total pressure taken as a reference P_{ref}, are presented in Tab.2. Pitot pressure probes and gas composition probes were used to measure Pitot pressure (P_{pitot}) and argon mass fraction (Y_{Argon}) distributions in several normal planes at different X/D_{cj} downstream locations.

	Center jet	Coflow jet	Ambient
$T_{tot}(K)$	297.9(±3.5)	294.3(±3.5)	294.6(±3.5)
$P_{tot}(Pa)$	615.86(±5.5)	P_{ref} =580.68(±4.4)	101.32(±0.6)

Table 2: Clifton & Cutler [1] initial flow conditions

4.2. Description of the computation

To cope with the axisymmetric geometry of the experiment, an O-H grid topology is adopted to avoid a singularity on the axes (see Fig.4c). N_θ =360 points are clustered in the azimuthal direction yielding an angular resolution $\Delta\theta = 1°$. The grid point distribution is refined in the mixing layer areas (see Fig.4b), especially for the air/argon one, with $N > 50$ points in the thickness of the mixing layer δ_{argon} (where δ_{argon} denotes the thickness of the zone where $0.01 < Y_{argon} < 0.99$) to ensure a good resolution of the large turbulent scales driving its dynamics. The computational domain is extended to 150 center jet diameters (D_{cj}) along the streamwise direction and more than $20D_{cj}$ radially (see Fig.4a). The mesh contains 165.10^6 cells overall.

To assess the importance of the incoming boundary layers in the development of the jets, two computations were run, one (called ZDES C1) using ZDES mode 2 (2020) [2] everywhere and another one using mode 3 of the ZDES (called ZDES C2) including special treatments to provide stimulated boundary layers (SBL).

As mentioned in Sec.2.3, within ZDES mode 2 (2020) the whole attached boundary layers are treated in RANS mode and the switch from RANS to LES in free shear layers is set automatically by the model

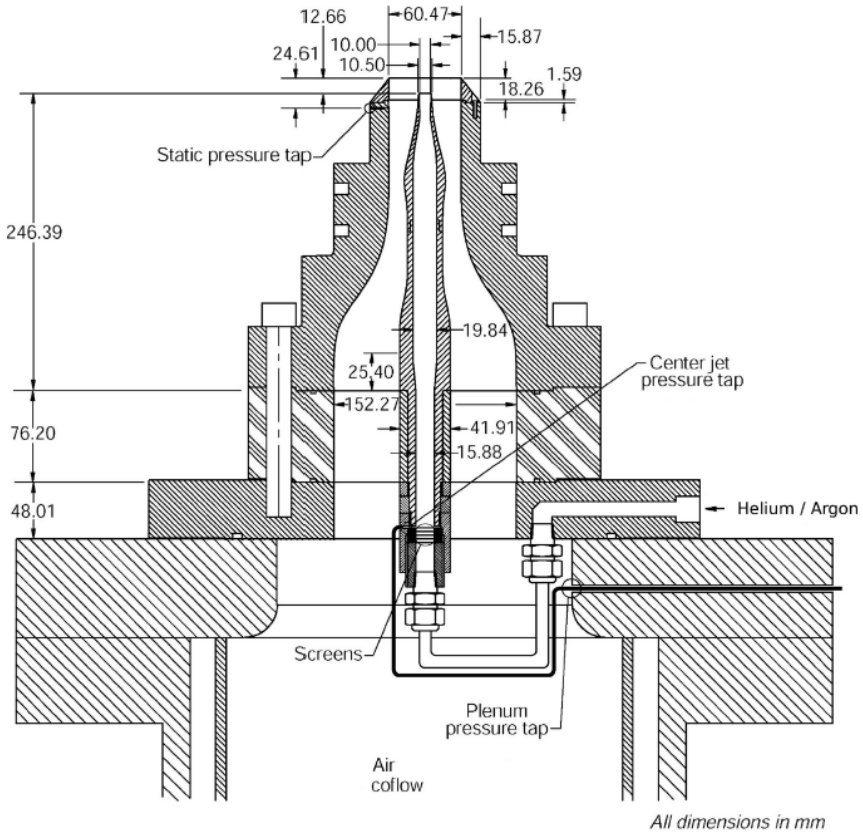

Figure 3: Clifton & Cutler [1] experimental setup.

itself. Conversely, ZDES mode 3 is built to treat the outer part of a boundary layer in LES mode. Thus, in order to compute an attached boundary layer (with a thickness $\delta(x)$) with this method, the meshing of the boundary layer areas have to respect several requirements classical of WMLES approaches [42, 43]. First, one has to ensure that around 100 cells are clustered in the boundary layer thickness, then criteria such as $\Delta x^+ \leq 200$, $\Delta(r\theta)^+ \leq 100$ and $\frac{\Delta x}{\delta} \leq 0.1$ (the superscript '+' denotes wall units which correspond to the adimensionalization performed using the mean shear stress τ_w, the kinematic viscosity ν_w and the density ρ_w, taken at the wall) have to be fulfilled in the boundary layer. Furthermore, it has been shown in [60] that the combination of a simple white noise at the inlet of the attached boundary layers with the dynamic forcing method proposed by Laraufie et al. [46] permits to obtain a self-sustained turbulent boundary layer. Besides, as recommended by the authors [46], the length of the forcing domain has to be $L_{forcing}= 8\delta_{in}$ where δ_{in} is the local boundary layer thickness at the inlet of the domain. Finally, the RANS/LES interface is set at $0.125\delta(x)$ where $\delta(x)$ is the boundary layer thickness provided by a preliminary RANS computation. This value ensures that the whole inner layer of the turbulent boundary layer is treated in RANS mode as advocated in [42, 43, 60, 62].

As shown in figure 5a, three attached boundary layers are involved in the present coaxial jets configuration. BL1 is the argon boundary layer developing on the center nozzle wall, BL2 is the air boundary layer developing on the lower wall of the coaxial nozzle and BL3 is the boundary layer developing on the upper wall of the coaxial nozzle. The $\Delta y^+ \approx 1$ condition is satisfied for all these attached boundary layers but they are treated

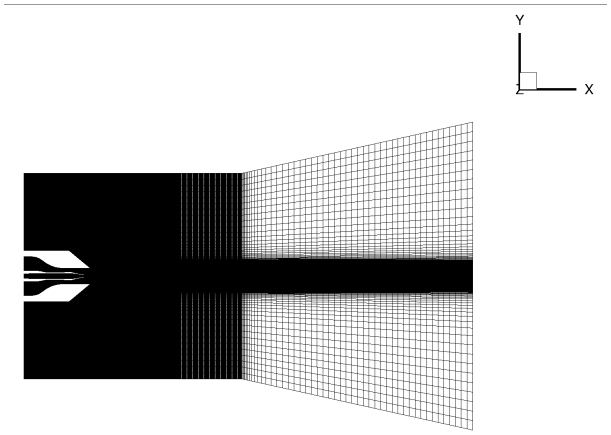

(a) Computational domain

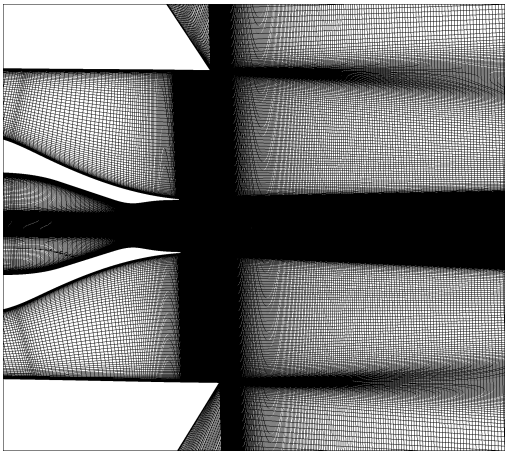

(b) Mesh distribution in the nozzles exit area

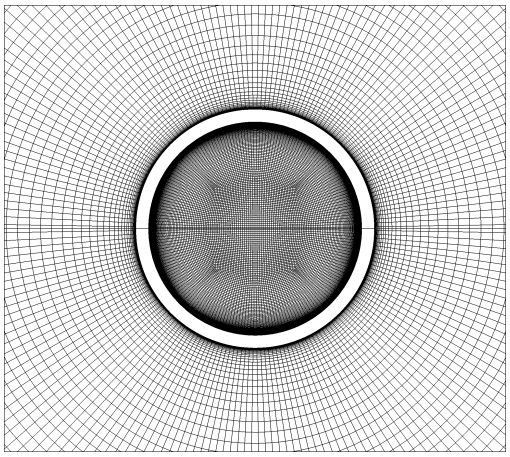

(c) O-H topology around the center nozzle axis

Figure 4: Mesh description

with different approaches within the ZDES C2 computation.

First, as we are particularly interested in the study of the mixing between argon and air, the upper air boundary layer BL3, which is assumed to have a weak impact on this mixing as it is not directly involved in the formation of the bi-species mixing layer with the center jet, is treated in URANS mode as in the ZDES C1 computations. Then, as preliminary RANS computations showed that the thickness of BL1 ($\delta_1(x)$) was around 8 times smaller than the thickness of BL2 ($\delta_2(x)$), the Mode 3 meshing requirements are retained only for the lower air boundary layer BL2. As reminded earlier, one of the asset of the ZDES lies in its capability to combine several modes (i.e. several levels of description) within the same calculation. In the present case, the grid in the azimuthal direction satisfies $\Delta(r\theta)^+ \leq 250$ for BL2 which is still coarse in a WMLES exercise [63], the objective is here more to assess the effect of turbulent inlet fluctuations on the development of mixing layers than the study of wall turbulence in the nozzle. Note that the cost of a WRLES (Wall-Resolved LES needing $\Delta(r\theta)^+ \leq 10$ and $\Delta x^+ \leq 40$ [64]) would be roughly $\frac{200}{40}.\frac{250}{10} \approx 125$ times ($i.e.(N_{xyz})_{WRLES} \approx 20.10^9$) more expensive than the present calculation ($i.e.$ $(N_{xyz})_{ZDES} \approx 165.10^6$)). To sum up, for the ZDES C2

computation, the air boundary layer BL2 is thus computed with a ZDES Mode 3 framework together with a dynamic forcing and the argon boundary layer BL1 is treated in URANS mode with the introduction of scaled white noise in the last cells before the nozzle exit to emulate turbulent fluctuations. The differences in boundary layer turbulent content between the ZDES C1 and the ZDES C2 computations can be clearly seen in Fig.5b showing pseudo-schlieren instantaneous visualizations of the flow in the center nozzle area.

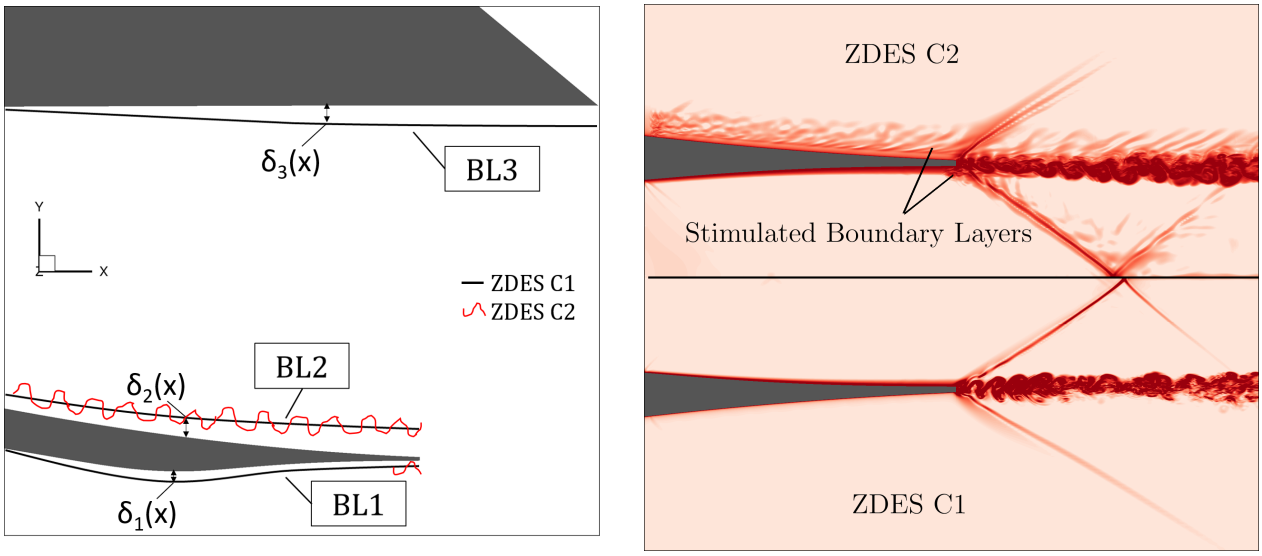

(a) Boundary layers of the coaxial jets (not to scale)

(b) Boundary layers treatment for the two ZDES computations

Figure 5: Treatment of the nozzles boundary layers

4.3. Numerical setup

As explained in Sec.3.4.3, several thermodynamic properties have to be defined in order to run a bi-species computation (see Table3). Furthermore for the mixture, the Schmidt number Sc between air and argon is set to 0.8 [65, 66] and as suggested in [17] the turbulent Prandtl number Pr_t is set to 0.9. Sc_t is set to 0.5 knowing that a previous study has shown that conversely to RANS methods, a weak dependence to Sc_t values is observed for scale resolving simulations[16].

	Air	Argon
μ_0 (N.s/m^2) [67]	$1.716.10^{-5}$	$2.125.10^{-5}$
T_0 (K) [67]	273	273
S (K) [67]	110.4	144
γ [68]	1.4	1.67
c_v (J/kg) [68]	717.5	312.4
Pr [68]	0.72	0.67

Table 3: Properties of the two exhaust gases

For the ZDES computations, the convective fluxes are computed thanks to the presented hybrid scheme [28] and a Koren MUSCL reconstruction. The timestep for ZDES is set to $\Delta t_{CFD} = 5.10^{-8} s$ thus enabling to ensure that $CFL = \frac{|u+c|\Delta t_{CFD}}{\Delta_n} < 10$, with Δ_n the radius of the inscribed sphere inside a cell, everywhere in the inner mixing layer. Note that the same time-step was retained by Baurle et al. [17]. Besides, 5 sub-iterations (n_{si}) are used for each iteration to obtain a decrease of inner residuals of at least one order. Transient and useful data sampling chosen for this coaxial jet flow vary between authors. As an example, Baurle et al. [17] chose to let the flow develop during two whole domain flow-through time ($T_{transient} * \frac{U_o}{D_{coflow}} \approx 48$ i.e. $T_{transient}$=6 ms) before computing statistics over a 1.5 ms period ($T_{average} * \frac{U_o}{D_{coflow}} \approx 12$). Troshin et al. [19] chose a 2.4 ms transient period ($T_{transient} * \frac{U_o}{D_{coflow}} \approx 19$) and a 12 ms period ($T_{average} * \frac{U_o}{D_{coflow}} \approx 96$) for ensemble average. In this study we chose to let the flow develop during 6 ms ($T_{transient} * \frac{U_o}{D_{coflow}} \approx 48$) before using another 6 ms period ($T_{average} * \frac{U_o}{D_{coflow}} \approx 48$) to perform time average. The flow field was then averaged azimuthally for comparison with experimental measurements and previous computations.

The simulations are performed on 336 Intel Xeon "Broadwell" processors and the CPU cost per cell per iteration is about $4.86.10^{-6}$ s.

5. Computational Results

5.1. General description

In the study of the present configuration, the observation of the mixing layers developing between the argon center jet and the air coaxial jet (inner mixing layer) with a convective Mach number $M_{c_i} = 0.16$ and between the air coaxial jet and the ambient air (outer mixing layer, $M_{c_o} = 0.77$) is of primary interest. To do so, a pseudo-schlieren snapshot of the flow where the locations of experimental probing stations used in this study are identified with vertical rakes is first presented in Fig.6. Note that this overall view has been obtained with the ZDES C1 computation (though not shown here, similar snapshots are provided by the ZDES C2 computation).

This view first enables to distinguish the formation of shock/expansion wave patterns tending to equalize the pressure between the two jets at the exit of the center nozzle. This compressible flow structure justifies the use of the hybrid scheme presented in Sec.3.1.3. Indeed, the numerical methods employed for such a flow have to be locally robust enough to capture the shocks while ensuring a low numerical dissipation in the vortical areas to properly resolve turbulent structures. Then, one can observe the growth of the two annular mixing layers driven by the formation of large scale structures. Due to a greater nozzle exit diameter and a higher velocity difference between its upper (ambient air) and lower (coaxial jet) streams, the outer mixing layer presents a growth rate significantly larger than the one for the inner mixing layer. Indeed, the inner mixing layer appears to be gradually perturbed by the outer mixing layer from $X/D_{cj} \approx 20$ (between the 4^{th} and the 5^{th} stations) until it is completely merged into a single wake flow for $X/D_{cj} > 35$.

An overview of the turbulent content in the mixing layers generated by the simulations is displayed in Fig.7 showing an iso-contour of the Q-criterion [69] coloured by the mass fraction of argon. The annular outer

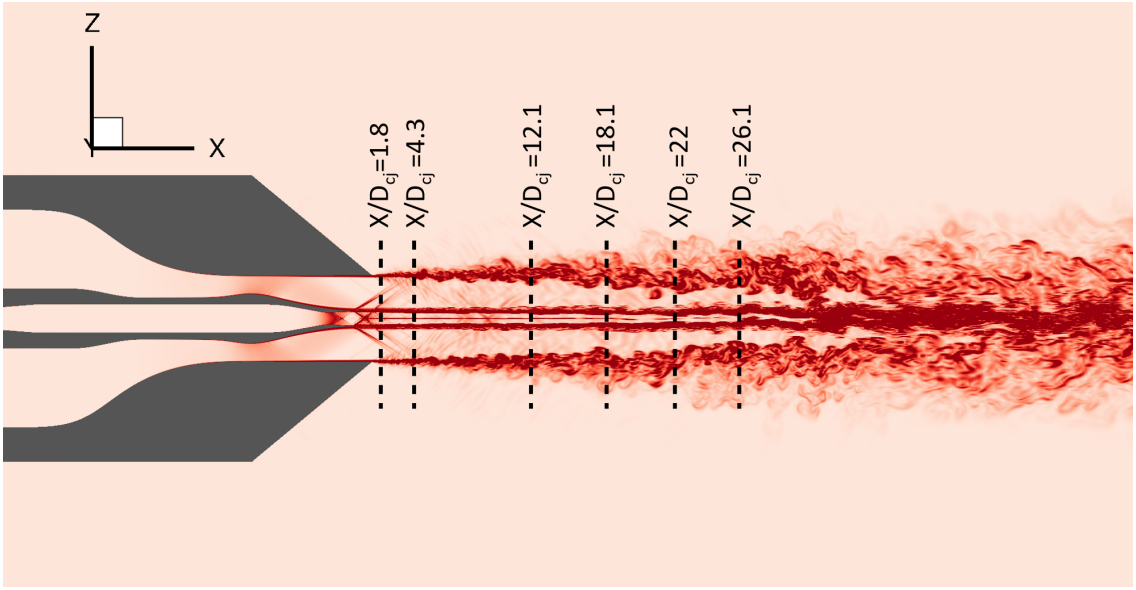

Figure 6: Instantaneous visualisation of the coaxial jets (ZDES C1)

mixing layer has been cut to reveal the inner one. For the outer mixing layer, the observed coherent structures in its early stages can be related to the descriptions given in [70, 71] for round jets mixing layers driven by Kelvin-Helmotz instabilities. Indeed, one can distinguish vortex-ring structures from the nozzle with the scale of these rings and the separation between the rings increasing as they move downstream. This growth is generally attributed to the coalescence of neighbouring rings. This pattern is however rapidly distorted as rings break up into three dimensional structures convected in the streamwise direction. As the convective Mach number of the outer mixing layer can be estimated as $M_{c_o} = 0.77$, this rapid loss in azimuthal coherence may be attributed to oblique instabilities characterizing compressible mixing layers (e.g. $Mc > 0.6$) [72, 73]. It is worth noticing that there is no delay in the formation of instabilities with the present ZDES Mode 2 (2020).

To assess the extent of these two mixing layers, Clifton and Cutler [1] provided Pitot pressure (P_{pitot}) radial distributions at several X/D_{cj} stations. The local Pitot pressure is indeed relevant to examine shear flows as it is related to the local pressure, Mach number and specific heat ratio of the flow $P_{pitot} = f(P, M, \gamma)$ through the isentropic definition of stagnation pressure and through the Rayleigh Pitot tube formula [74] downstream a normal shock. As an example, the relative Pitot pressure distribution at a station located at X/D_{cj}=4.3 is shown in Fig.8. In this figure, the inner mixing layer corresponds to the Pitot pressure deficit occurring in the $0.3 \leq r/D_{cj} \leq 0.7$ range between the argon jet and the air jet. This deficit is due to the convection of low total pressure flow from the nozzles boundary layers and from a small recirculation zone developing behind the center nozzle base [17]. The outer mixing layer corresponds to the Pitot pressure drop occurring in the $2.6 \leq r/D_{cj} \leq 3.4$ zone between the air jet and the ambient air. One can observe that both present computations provide very satisfactory predictions for this station in comparison to experimental results. As the focus is put here on the evaluation of a bi-species numerical framework, Pitot pressure distributions presented for the following stations in the next sections are zoomed around the inner mixing

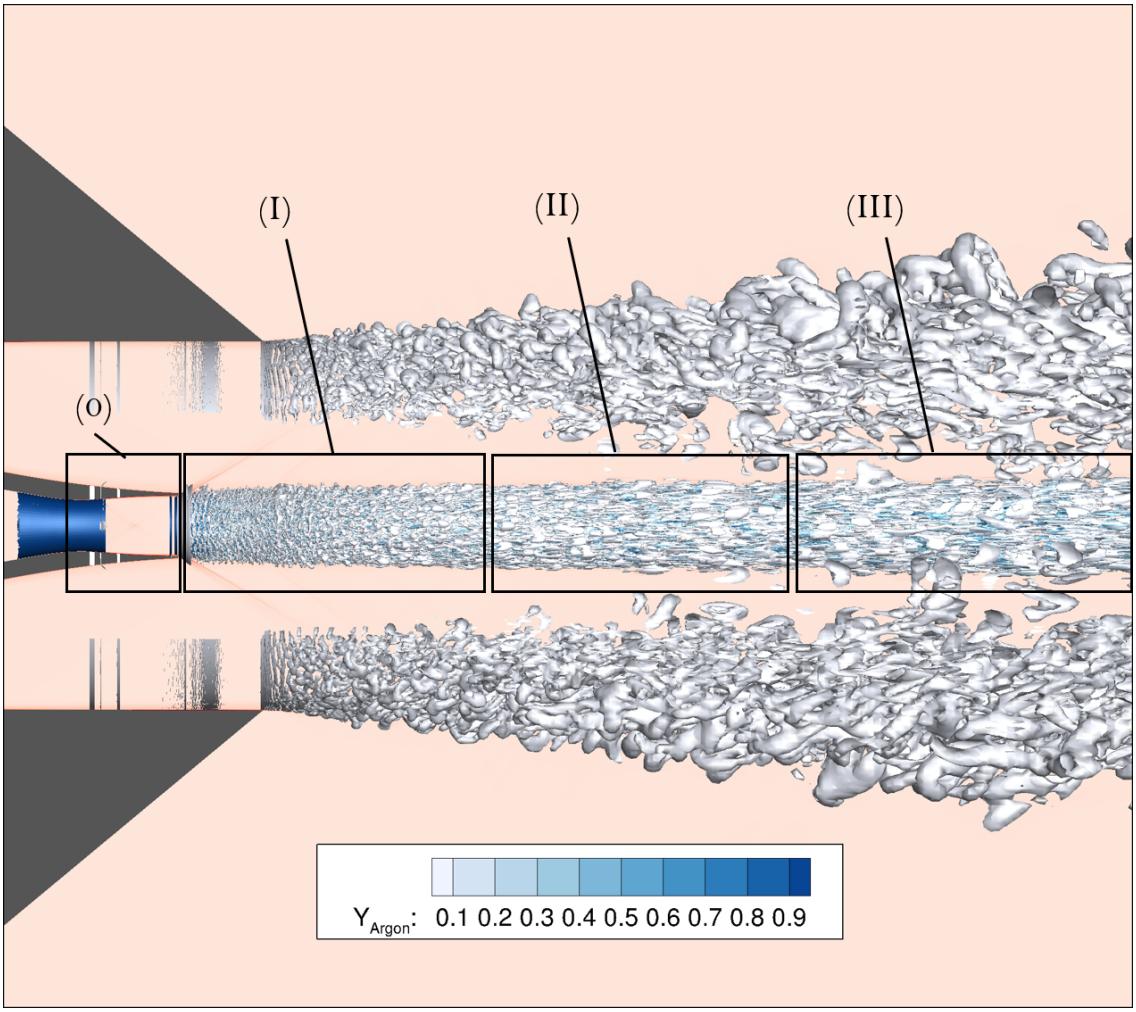

Figure 7: Instantaneous visualisations of the coaxial jets thanks iso-Q criterion surfaces: $\frac{Q \times U_o^2}{\delta_{BL2}^2} = 0.0025$. (0) Boundary layers, (I) Near field, (II) Intermediate region, (III) Interference area. (ZDES C1).

layer area ($r/D_{cj} \leq 2$).

The inner mixing layer developing between the argon jet and the air jet presents a lower convective Mach number $M_{c_i} = 0.16$ than the outer one. An average view of argon mass fraction distribution obtained with the ZDES C1 computation shown in Fig.9a enables to visualize the gradual mixing occurring at the interface between the two gases. To compare the predicted growth of the inner mixing layer with the experimental results of Clifton and Cutler [1], Fig.9b presents the radial locations of the 1% and 99% argon mass fraction boundaries of the inner mixing layer for the six studied stations. It can be noticed that both C1 and C2 computations provide predictions in good agreement with experimental results for the outer boundary ($Y_{Argon} = 0.01$) and for the near field of the inner boundary ($Y_{Argon} = 0.99$) whose extent is however underestimated for x/$D_{cj} \geq 18.1$.

As indicated in Fig.7, to provide a thorough investigation of the flow, the analysis will be divided in three parts corresponding to three characteristic zones of the inner mixing layer. The focus is first put on the near field area (I) ($0 < X/D_{cj} < 10$) where an inner Air/Argon mixing layer develops. Then, the intermediate region (II) ($10 \leq X/D_{cj} < 20$) is briefly considered before getting interested in the interference area (III)

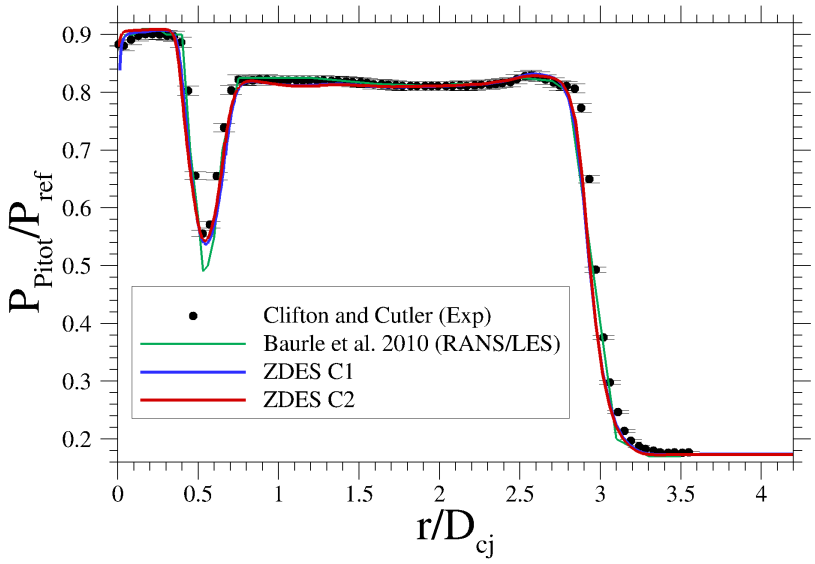

Figure 8: Radial distributions of relative Pitot pressure obtained with ZDES computations at the station X/D_{cj}=4.3. See Table 2 for the definition of P_{ref}.

$(20 \leq X/D_{cj})$ where the Air/Argon mixing layer is gradually perturbed by the outer mixing layer.

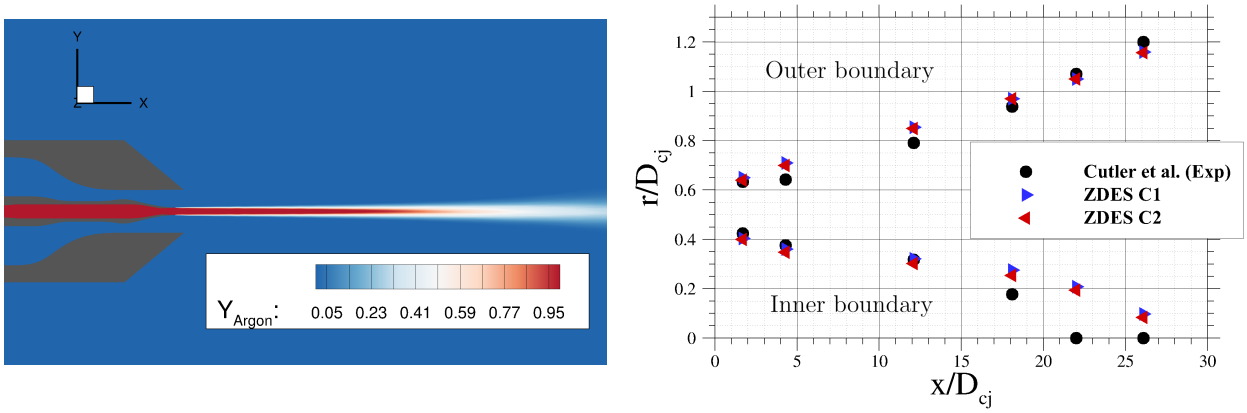

(a) Averaged Y_{argon} distribution (ZDES C1)

(b) Radial locations of the 1% and 99% argon mass fraction boundaries. See Fig6 for locations.

Figure 9: Averaged Y_{argon} distributions obtained with the ZDES computations

The experimental time averaged Pitot pressure and argon mass fraction measurements obtained in [1] are used to appraise the computational results at two stations for each mentioned zone. Present results are also compared with previously published RANS/LES results from Baurle et al. [17] and SST-DDES results from Troshin et al. [19].

5.2. Near field ($0 < X/D_{cj} < 10$)

This section concerns the investigation of the inner mixing layer development in the proximity of the center nozzle (see region I in Fig.7).

5.2.1. Flow topology

Let us be reminded that the thickness of the center nozzle lip is nearly equal to two times the inner boundary layer thickness (see Fig 5b) and is thus around 4 times smaller than the air boundary layer. As described in [75], for coaxial jets with a velocity ratio r_u close to unity and separated by a thick wall, a wake instability (causing a vortex shedding phenomenon) may compete with the K-H instability and modulate the dynamics of the flow. A small recirculation region may furthermore form behind the lip base [76]. Figure 10 displays the instantaneous distribution of relative velocity (u/U_i) in the very first stages of the inner mixing layer. In particular, one can recognize the formation of a recirculation bubble and alternate vortices characteristic of the vortex shedding phenomenon.

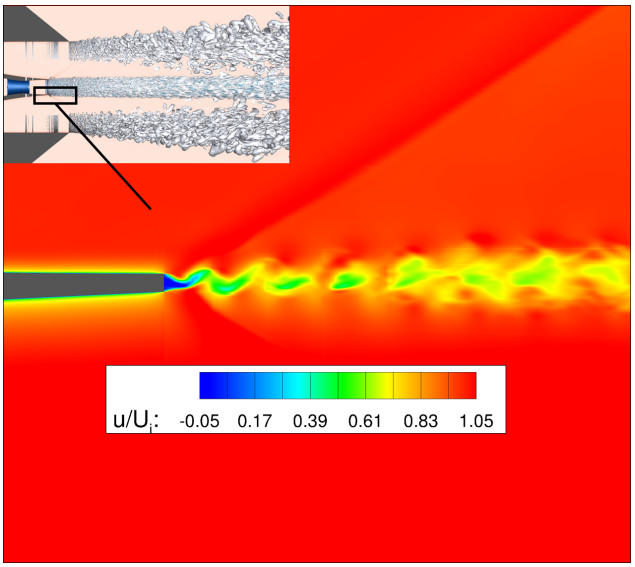

Figure 10: Distribution of relative velocity at the onset of the inner mixing layer.

Alternating argon-filled and air-filled azimuthal rollers are visible in Fig.11a displaying the coherent structures organising the flow in the nozzle area for the ZDES C1 computation. They also tend to indicate the occurrence of a vortex shedding phenomenon. For the ZDES C2 computation which includes SBL (Stimulated Boundary Layers) (Fig.11b), this pattern is perturbed by the presence of coherent three dimensional structures from the incoming air boundary layer. This figure shows again the interest of the present numerical flux (eq.51) that adapts its level of dissipation to permit the resolution of turbulent structures in both attached and free shear flows while ensuring the capturing of the shocks. To complete the comparison in the vicinity of the nozzle, instantaneous pseudo schlieren visualizations are shown in Fig.12 for transversal planes located at X/D_{cj}=-0.03 and 0.5. Figures 12a and 12c show the incoming nozzle boundary layer treated in URANS mode (ZDES C1) and WMLES mode (ZDES C2), respectively. In the latter case, the small scale disturbances issued from the upstream boundary layer are amplified by the mixing layer instabilities. Looking at the organisation of the flow in the very first stages of the mixing layer (X/D_{cj}=0.5, see Fig.12b and Fig.12d), the presence of turbulent fluctuations coming from the attached boundary layers appears to induce a decrease in azimuthal coherence and a reduction in the size of the large scales driving the mixing between the two streams.

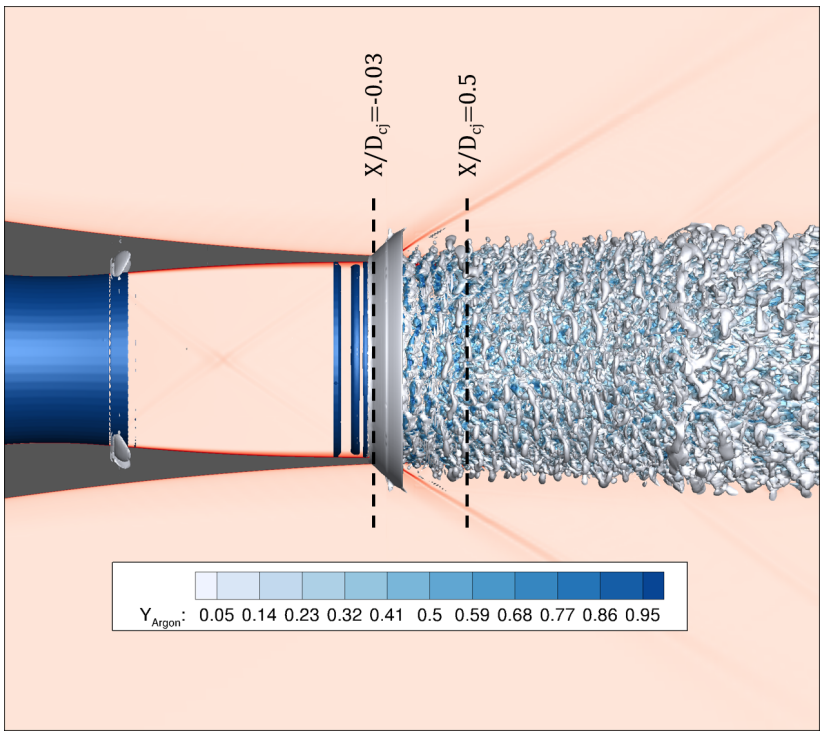

(a) ZDES C1

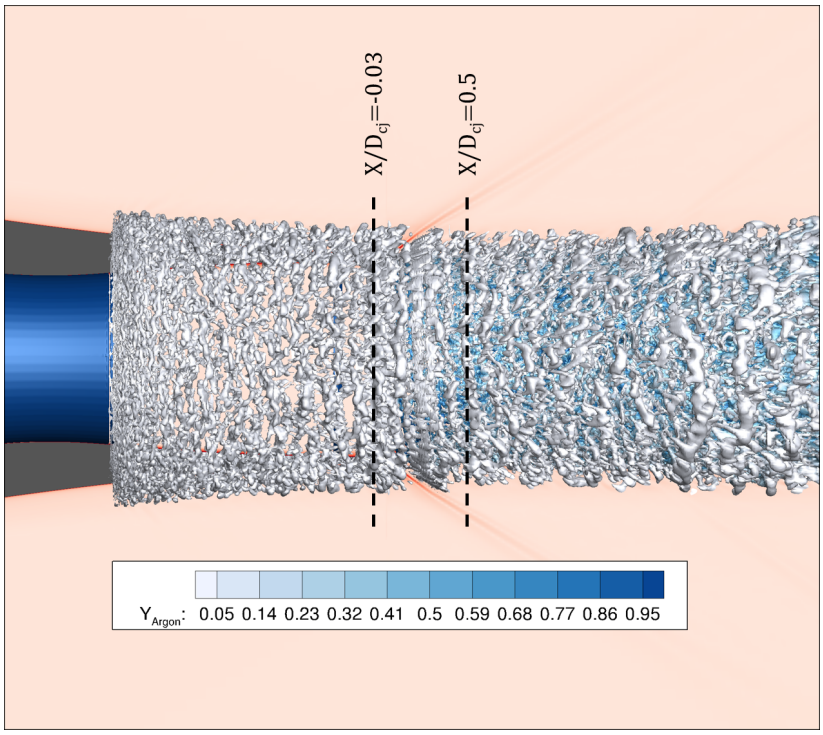

(b) ZDES C2

Figure 11: Iso-surfaces of Q criterion colored by Y_{Argon} in the boundary layer (0) and near field (I) regions. See Fig.7 for the location of these regions. The indicated transversal slices are shown in Fig.12.

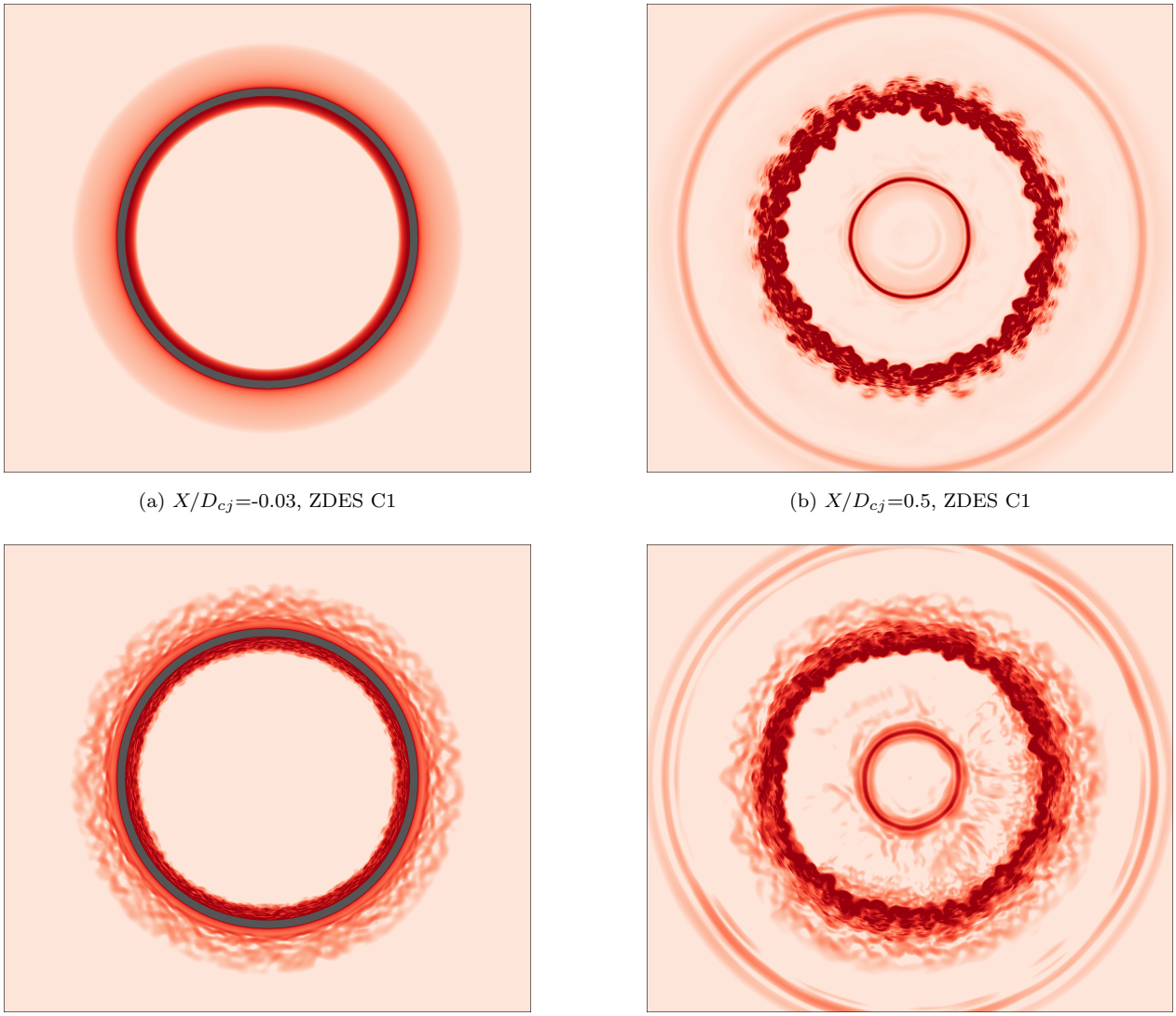

(a) X/D_{cj}=-0.03, ZDES C1

(b) X/D_{cj}=0.5, ZDES C1

(c) X/D_{cj}=-0.03, ZDES C2

(d) X/D_{cj}=0.5, ZDES C2

Figure 12: Pseudo schlieren visualization of the flow for transversal planes located at X/D_{cj}=-0.03 and 0.5.

5.2.2. Time averaged results

In this section, the predictions obtained with the two computations C1 and C2 in terms of averaged results are assessed in order to investigate how the generation of turbulent content affects the mixing process between the two gases.

Time averaged results are first displayed at two stations located in the near field region at X/D_{cj}= 1.8 (Fig.14) and X/D_{cj}= 4.3 (Fig.15). The structure of the mixing layer in this area can be inferred from the radial distribution of axial velocity displayed in Fig.13. Due the merging process of the two boundary layers and the total pressure loss caused by the recirculation zone behind the nozzle lip, a low velocity zone $\frac{u}{U_i} < 1$, corresponding to the wake of the nozzle lip, exists between the two jets. Moving radially from the center line a velocity decrease ($\frac{\partial u}{\partial r} < 0$) precedes the expected velocity increase ($\frac{\partial u}{\partial r} > 0$) due to the entrainment by the outer jet. Such a velocity profile is coherent with the experimental results of Mehta [77] who studied

the influence of a wake of the splitter plate on the development of mixing layers for velocity ratios $r_u < 2$. Those experimental results furthermore showed that the velocity defect, increases when the velocity ratio gets closer to 1, as does the streamwise distance over which it is still discernible. For coaxial jet set-ups with thick nozzles and velocity ratios $r_u < 2$, other authors [78, 79] also reported the presence of a low velocity region dividing the mixing layer into two zones with different turbulent mixing properties.

The radial distributions of Reynolds stresses provided by the present computations compare qualitatively with the ones obtained by Mehta on a similar configuration [77] and enable to distinguish these two zones. Indeed in Fig.14c and Fig.15c, one can observe that, as described by Mehta [77] for mixing layers influenced by the splitter plate wake, the streamwise velocity fluctuations (u_{rms}) profiles exhibit two distinct peaks. The radial velocity fluctuations (v_{rms}) profiles are asymmetric and the levels of both these velocity fluctuations decrease in the streamwise direction (from Fig.14c to fig.15c). The Reynolds shear stress profiles shown in Fig.14d and Fig.15d are also coherent with the profiles reported in [77] as they are divided into two shear zones $< u'v' > \geq 0$ and $< u'v' > \leq 0$ and the peak values of which decrease in the direction of the flow.

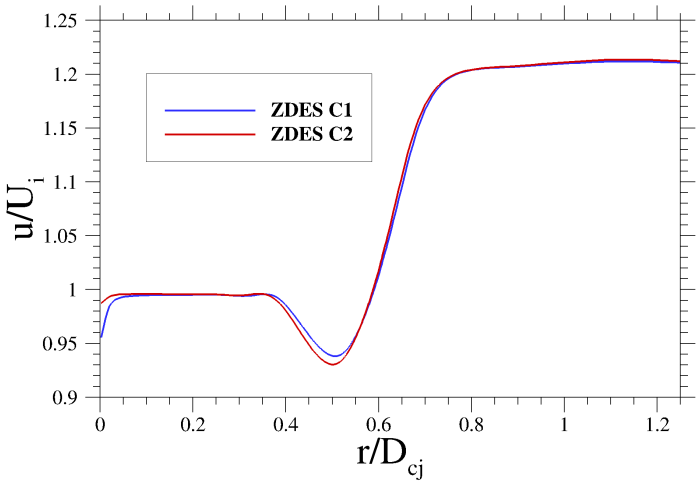

Figure 13: Radial distribution of axial velocity at X/D_{cj}= 4.3

Looking at the evolution of relative Pitot pressure distribution from Fig14a to Fig.15a, one can note that in the direction of the flow, the pressure deficit zone broadens and its minimum value increases ($(\frac{P_{pitot}}{P_{ref}})_{min} \approx$ 0.45 for X/D_{cj}=1.8 and $(\frac{P_{pitot}}{P_{ref}})_{min} \approx 0.55$ for X/D_{cj}=4.3) as the mixing layer grows and the two streams merge. In practice, both present computations C1 and C2 allow for a good representation of the physical phenomenon observed in the experiment. A fair agreement is also obtained for the evaluation of the argon mass fraction (Fig.14b and 15b) even if a minor overestimation of Y_{argon} is observed on the outer side ($r/D_{cj} > 0.5$) of the mixing layer.

Besides, it can be noticed in Fig.14d and Fig.15d that calculations C1 and C2 differ in the assessment of the turbulent mixing process as they produce different extremum values and spatial extents for the Reynolds stress peaks ($< u'v' >$). In practice, the introduction of fluctuations inside the attached boundary layers in the ZDES C2 computation induces both an increase of $< u'v' >$ extremum values and a shift in their radial locations. Those differences have discernible consequences on the Y_{argon} averaged radial distribution at the

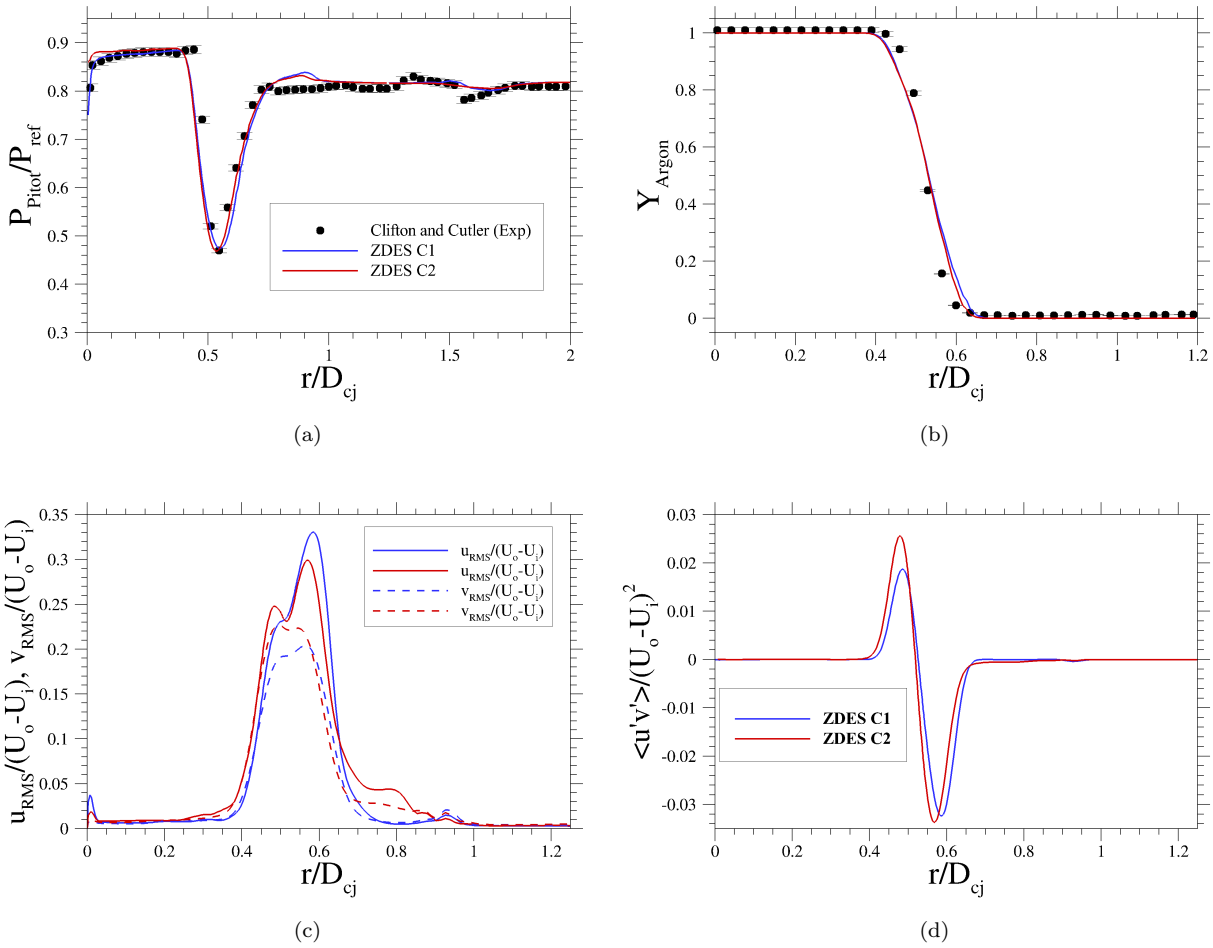

Figure 14: Radial distributions of relative Pitot pressure (a), argon mass fraction (b), rms velocities (c) and total Reynolds shear stress (d) obtained with ZDES at the station X/D_{cj}=1.8.

station X/D_{cj}=1.8. The overestimation of Y_{argon} is indeed smaller with the ZDES C2 computation than with the ZDES C1 computation and this might be related to the smaller spatial extent of the shear stress peak observed on the outer side of the mixing layer for the case C2 in Fig.14d.

The comparison of current computations with RANS/LES results from Baurle et al.[17], indicates a better agreement with the experimental Y_{argon} (Fig.15b) distribution at the station X/D_{cj}=4.3, though an overestimation of the Pitot pressure drop (Fig.15a). This can be related to the fact that in [17], fully 3-D turbulent structures are only observed in the mixing layer for $X/D_{cj} > 10$ whereas such structures are already found in the near field with the present computations (Fig.11). Let us be reminded that ZDES mode 2 (2020) has been designed to allow a fast development of resolved turbulence when switching in LES mode. The use of a finer grid may also explain the differences between present results and those published in [17].

Overall, the bi-species ZDES framework presented in this paper provides satisfying predictions of the mixing process occurring in the near field area of the argon-air mixing layer.

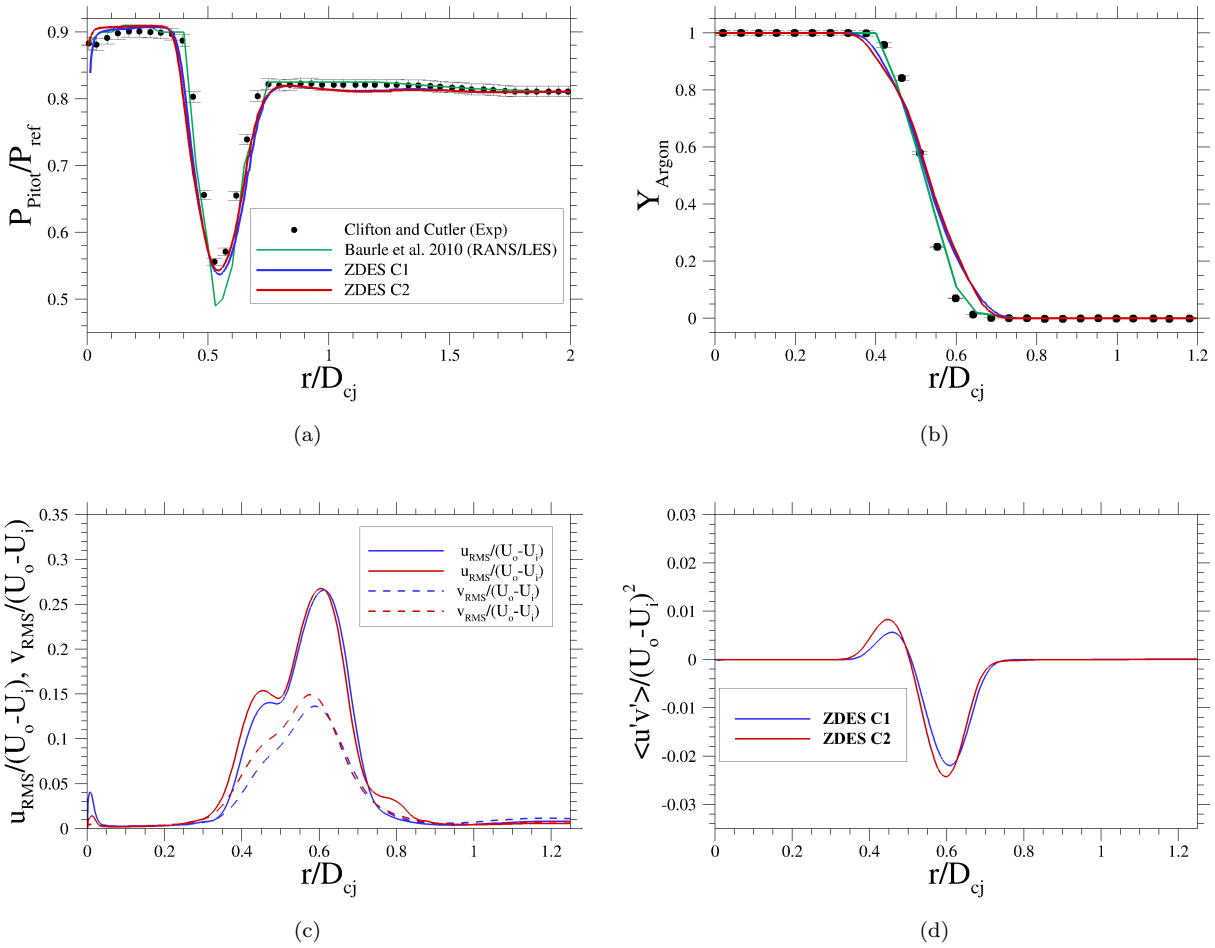

Figure 15: Radial distributions of relative Pitot pressure (a), argon mass fraction (b), rms velocities (c) and total Reynolds shear stress (d) obtained with ZDES at the station X/D_{cj}=4.3.

5.3. Intermediate region ($10 < X/D_{cj} < 20$)

An instantaneous snapshot of the flow in the intermediate region is given in Fig.16. One can note the predominance of longitudinal coherent structures organising the flow in this area and the stability of the inner mixing layer envelop which does not seem yet perturbed by the outer mixing layer. Minor differences have been observed between the ZDES C1 and C2 computations in this region of the flow.

In this zone, located at more than 10 diameters downstream of the nozzle area, the low velocity region between the two jets is almost recovered and the velocity grows radially from U_i to U_o as in a canonical developing mixing layer (see Fig.17). Looking at the normal (Fig.18c and Fig.19c) and the shear stresses (Fig.18d and Fig.19d) distributions, one can acknowledge that they tend towards classical gaussian-like curves expected in developed self-similar mixing layers [80]. In addition, the observed peak levels obtained for second order statistics can be compared with data from literature on fully developed mixing layers with similar convective Mach numbers ($M_{c_i} = 0.16$). Such a comparison is achieved thanks to the review of experimental results provided by Tan et al. [81] for M_c=0.2 mixing layers. First, the peak values of Reynolds shear stress provided by the present computations in the intermediate area are $(\frac{|<u'v'>|}{(U_o-U_i)^2})_{max} =$

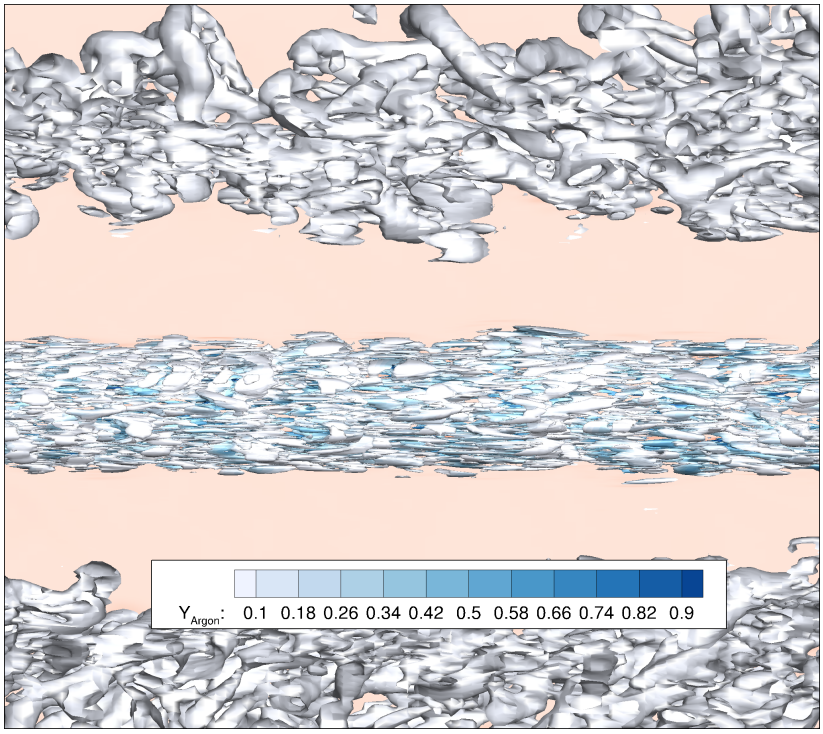

Figure 16: Coherent structures inside the mixing layers in the intermediate region (II) (ZDES C1 computation). See Fig.7 for the location of this region.

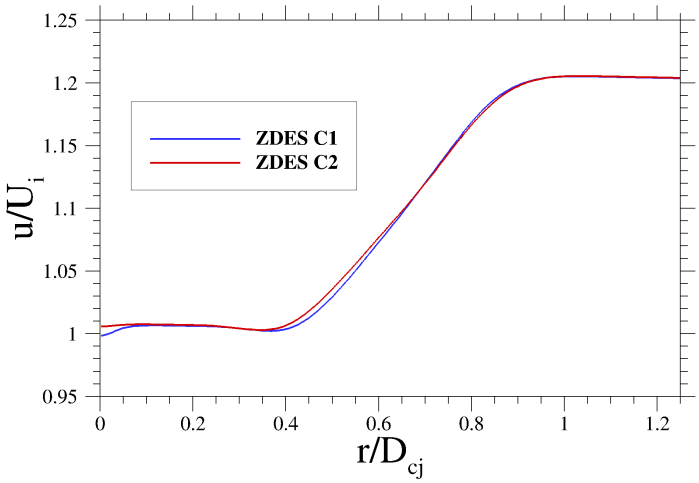

Figure 17: Radial distribution of axial velocity at X/D_{cj}= 18.1

0.021 (X/D_{cj}=12.1) and 0.024 (X/D_{cj}=18.1) for the ZDES C1 computation and $(\frac{|<u'v'>|}{(U_o-U_i)^2})_{max} \approx 0.025$ (for both locations) for the ZDES C2 computation, respectively. These values are similar to those reported in [81] ($(\frac{|<u'v'>|}{(U_o-U_i)^2})_{max} \in [0.016, 0.021]$) for plane supersonic mixing layers. Then, the streamwise velocity fluctuations peak values predicted by the ZDES computations $(\frac{u_{rms}}{(U_o-U_i)})_{max} \in [0.27, 0.29]$ corroborate those reported in [81] $(\frac{u_{rms}}{(U_o-U_i)})_{max} \in [0.2, 0.24]$. Finally, the computed transverse velocity fluctuations $(\frac{v_{rms}}{(U_o-U_i)})_{max} \in [0.13, 0.15]$ compare fairly well with the value $(\frac{v_{rms}}{(U_o-U_i)})_{max} = 0.15$ measured in [82]. Overall, the level of turbulent intensity computed by the two ZDES computations in the intermediate region of the inner mixing

layer appears coherent with the experimental measurements for fully developed mixing layers. The minor discrepancies can be first attributed to the higher convective Mach number of the mixing layers described in [81]. Second, it is shown in [77] that the turbulent intensity level of a mixing layer grows as the velocity ratio r_u gets closer to 1. The present velocity ratio r_u (=1.2) may thus be closer to 1 than the velocity ratios of the mixing layers studied experimentally (r_u >1.2). Then, the mixing layers studies reported in [81] all used air as the flowing gas for both streams. Thus, in the present study, the differences in density between the argon jet and the air jet might enhance the mixing between the two flows as mentioned in [83].

The observation of Reynolds stresses furthermore shows that for both stations studied in this region of the flow (X/D_{cj}=12.1 and 18.1), the introduction of turbulent content in the boundary layers induces a slight rise in turbulent mixing intensity but does not modify the shape of the turbulent fluctuations distribution as it was the case in the near field region. The effects of this increased turbulent mixing intensity can also be observed on time averaged Pitot pressure distributions (Fig.18a and Fig.19a) and on the time averaged argon mass fraction distributions (Fig.18b and Fig.19b) where ZDES C2 features a faster diffusion of argon particles into air than found with the ZDES C1 computation. Both present ZDES computations provide good agreements with experimental Pitot pressure profiles as they allow for improved predictions in comparisons with previous computations [17, 19]. The computed argon mass fraction profiles provide a good agreement with measures from [1] in the inner part of the mixing layer ($r/D_{cj} \leq 0.6$) but overestimate Y_{argon} in the outer part of the mixing layer. This local overestimation is in contrast with the overall under-prediction of turbulent mixing intensity reported in previous calculations [17, 19]. As previously discussed in Sec.5.2.2, such differences can be linked to the faster development of 3-D turbulent structures observed in the present computation in comparison with studies [17, 19].

5.4. Interference area ($20 \leq X/D_{cj}$*)*

This section is devoted to the investigation of the last zone of this flow mixing process. In the case of a single jet, the argon-air mixing layer would develop towards a self-similar turbulent flow. However, in the present case of coaxial jets, the development of the inner mixing layer is perturbed by the interaction with the outer mixing layer. More precisely, the inner mixing layer observed in Fig.20 appears to undergo large scale radial oscillations, breaking free from its quasi-cylinder external shape observed in the intermediate region. The increase in both Reynolds shear stress levels in the region r/D_{cj} >1.1 (Fig.22d and Fig.23d) and radial velocity fluctuations ($(\frac{v_{rms}}{(U_o-U_i)})_{max} > 0.15$ in Fig.22c and Fig.23c) in comparison with the intermediate region also shows the influence of the outer mixing layer on the mixing process between argon and air.

Looking at the averaged Pitot pressure distribution in this area (Fig.22a and Fig.23a), experimental results display an important decrease of the Pitot pressure in the core of the center jet (r/D_{cj} <0.25) in comparison with almost constant levels observed in the near field and intermediate regions. This decrease, associated with a strong reduction of the pressure deficit zone, can be attributed to two major effects. First, due to the previously mentioned radial oscillations of the whole inner mixing layer, a fixed experimental probe used for time-averaged measurements may acquire values corresponding to different relative radial positions inside the mixing layer. The sensitivity to the probe location may produce a radial averaging flattening extrema

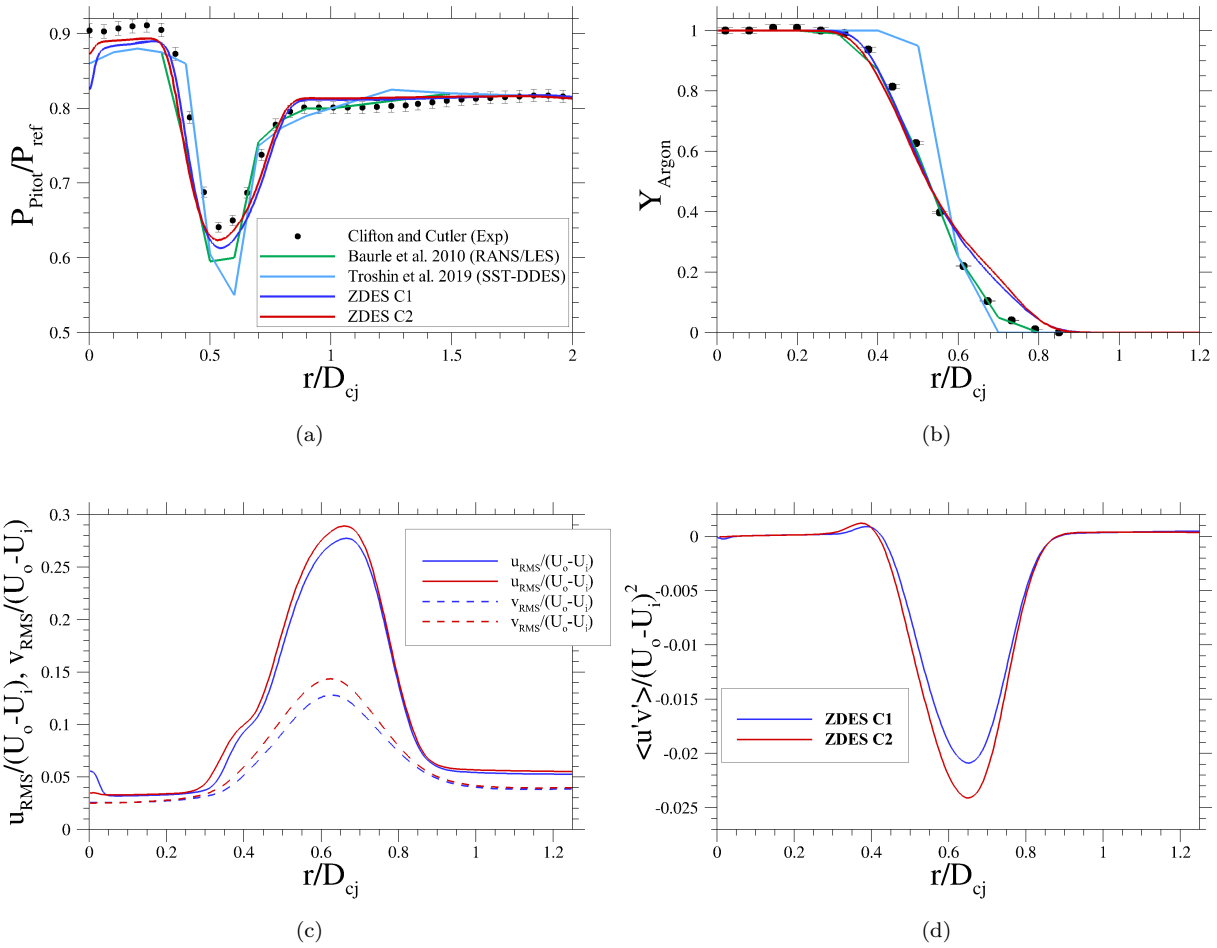

Figure 18: Radial distributions of relative Pitot pressure (a), argon mass fraction (b), rms velocities (c) and total Reynolds shear stress (d) obtained with ZDES at the station X/D_{cj}=12.1

values. Second, it could be related to an increase in turbulent mixing intensity near the center of the jet due to the transfer of turbulent kinetic energy from large turbulent scales located at the mixing layer boundary to smaller scales evolving in the center of the argon jet.

This decrease in Pitot pressure is not well captured neither by the present ZDES computations (165.10^6 cells) nor by previously published RANS/LES computations by Baurle et al. [17] (43.10^6 cells). These discrepancies could be partly due to an underestimation of the influence of the outer mixing layer or of the intensity of turbulent mixing in the center of the jet.

These potential discrepancies in the assessment of turbulent mixing have a smaller impact on argon mass fraction distributions. At the station X/D_{cj}=22 in Fig 22b, the present ZDES computations feature an improved agreement with experimental data compared to previous numerical studies [17, 19]. The agreement is particularly satisfying in the outer part of the mixing layer (r/D_{cj} >0.5). The under prediction of turbulent mixing in the center jet is however clearly visible for the argon mass fraction distribution shown in Fig.23b.

In fine, this study has shown that the capability to assess the physical phenomena driving the mixing in the center of the argon jet is particularly challenging. It has also been shown that the current ZDES

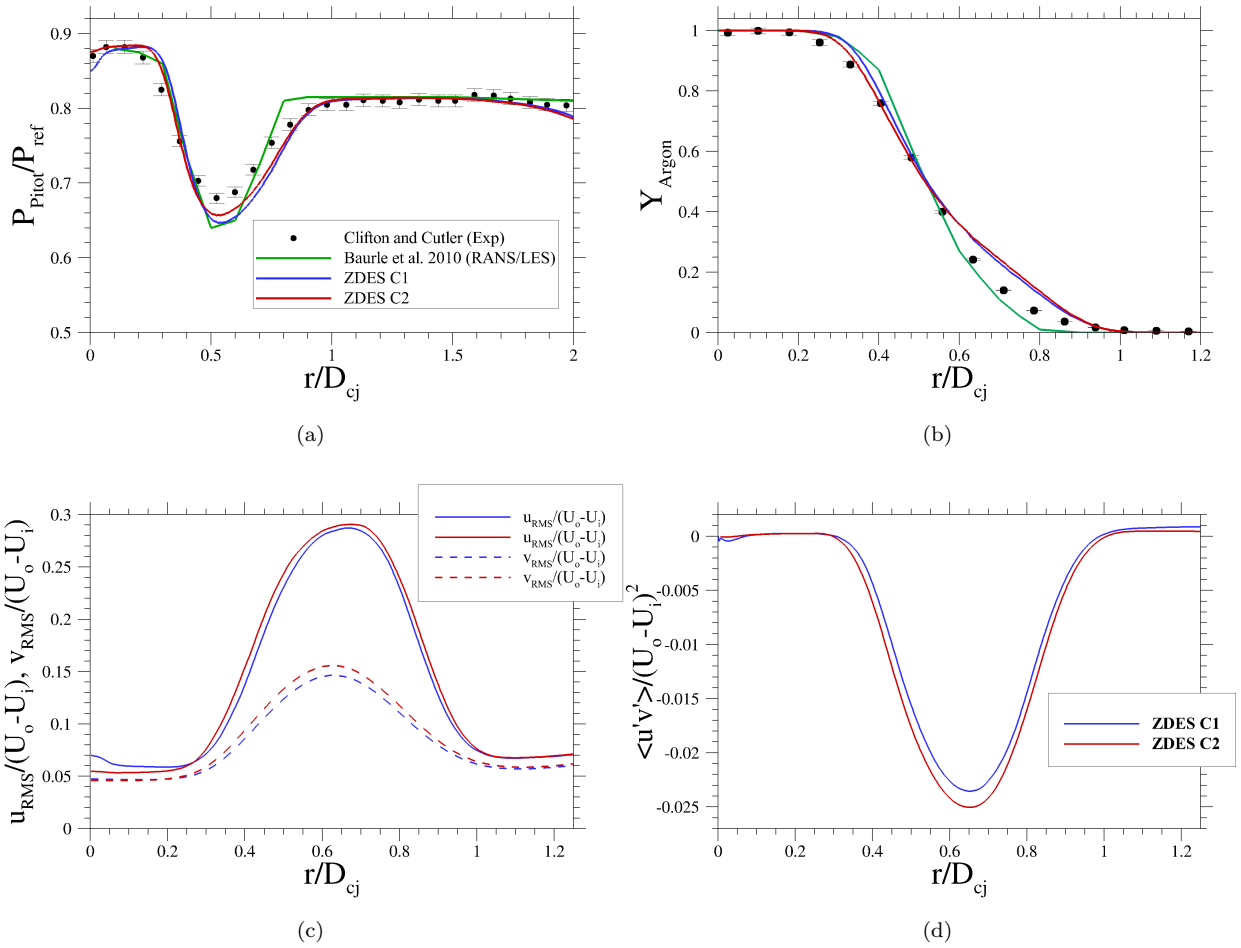

Figure 19: Radial distributions of relative Pitot pressure (a), argon mass fraction (b), rms velocities (c) and total Reynolds shear stress (d) obtained with ZDES at the station X/D_{cj}=18.1

computations permit a fair prediction for the outer part of of the mixing layer in the interference area.

6. Conclusion

A strategy for scale-resolving simulations of bi-species turbulent flows has been presented. The salient modelling hypothesis for two-species turbulent flow simulations are first reminded. The corresponding detailed discretized equations have then been thoroughly presented in the frame of a structured finite volume code based on a second order time accurate implicit integration scheme. A description of the main boundary conditions are briefly discussed. The calculation of the advective fluxes relies on an original low-dissipative version of the AUSM scheme that permits to capture shocks while ensuring a low numerical dissipation in the vortical areas to properly resolve turbulent structures.

Turbulence treatment is based on the advanced Zonal Detached Eddy Simulation (ZDES) technique that uses two main operating modes. The first one named mode 2 (2020) provides an "automatic" operating mode for which the switch between RANS and LES regions is dynamically set by the model itself. The second one (named mode 3) is the WMLES mode of ZDES where the outer layer of attached boundaries is resolved

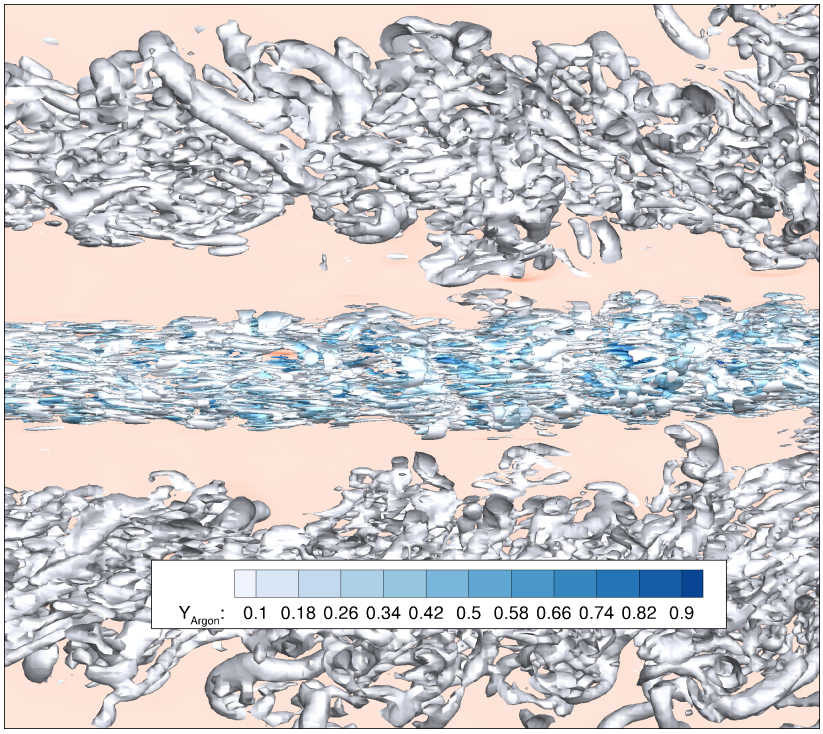

Figure 20: Coherent structures inside the mixing layers in the interference area (III) (ZDES C1 computation). See Fig.7 for the location of this region.

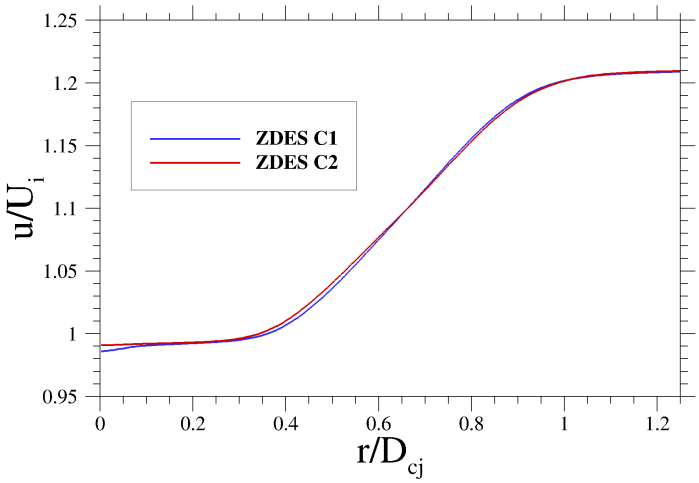

Figure 21: Radial distribution of axial velocity at X/D_{cj}= 22

conversely to its mode 2 counterpart where the whole attached boundary layer is treated in RANS. Within mode 3, turbulent boundary layers need to be fed with unsteady velocity fluctuations. In this study, a robust method based on a physically motivated combination of white noise to generate fluctuations at the inlet together with a dynamic forcing method is applied for the first time in a compressible curvilinear bi-species flow framework. This comprehensive framework has then been assessed on the well-known coaxial Air/Argon jet investigated experimentally by Clifton and Cutler [1] and compared on a 165×10^6 grid with previously published hybrid RANS/LES numerical works. Both instantaneous and time-averaged flow fields have been

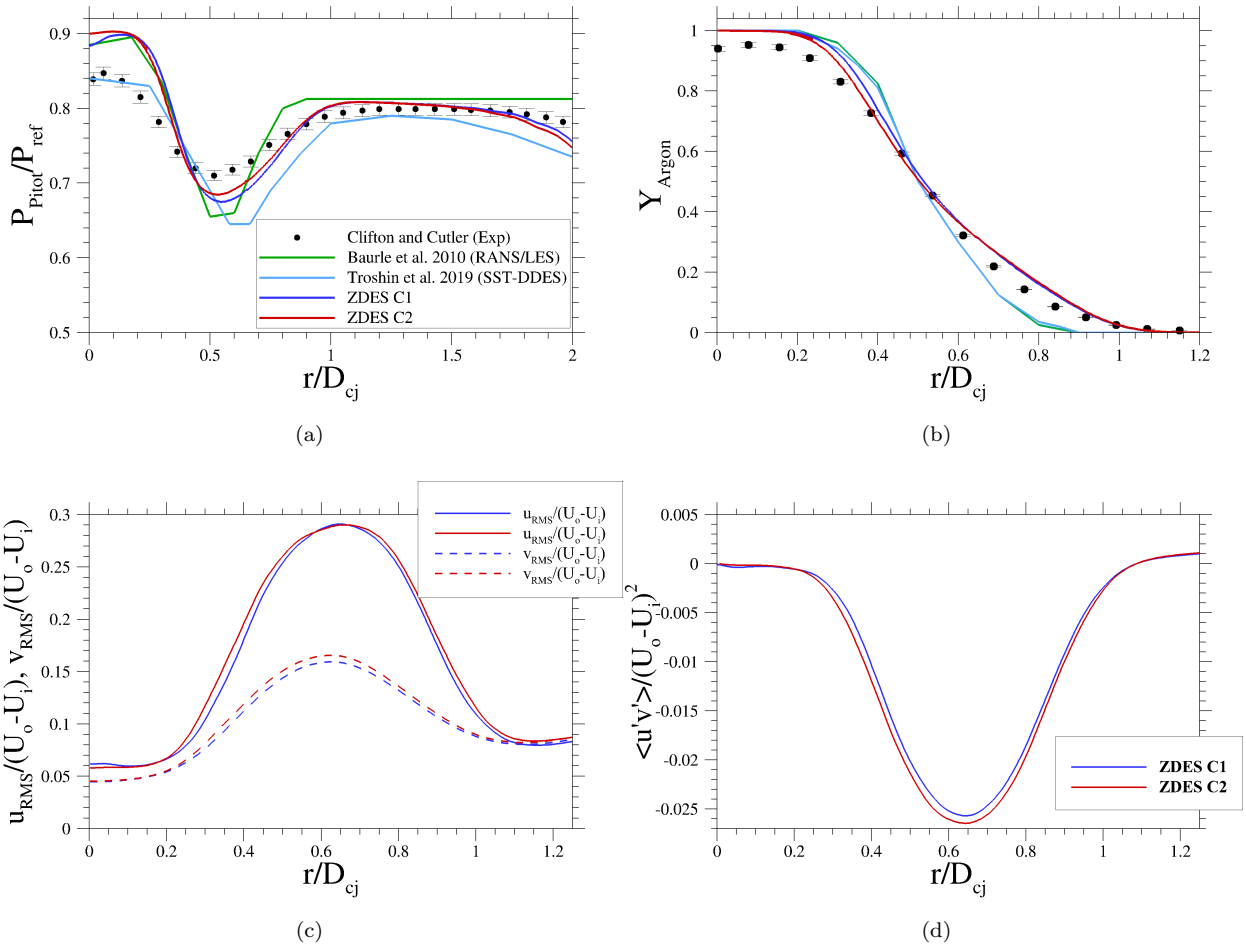

Figure 22: Radial distributions of relative Pitot pressure (a), argon mass fraction (b), rms velocities (c) and total Reynolds shear stress (d) obtained with ZDES at the station X/D_{cj}=22

thoroughly investigated. No delay in the formation of instabilities in the free-shear layers has been observed with the mode 2 (2020) of ZDES despite a RANS description of the incoming boundary layers. The taking into account of resolved turbulence in these attached boundary layers within ZDES Mode 3 permits a better prediction of the mixing process in the early stages of the mixing layer.

Because of the complexity to simulate the mixing process of bi-species turbulent flows, the use of hybrid RANS/LES methods will remain essential for a long time to address high-Reynolds curvilinear configurations involving attached turbulent boundary layers.

Acknowledgments

The authors wish to thank Professor Andrew Cutler for providing detailed parameters and results of the experimental studies, [27, 1]. The authors also wish to thank R. Collercandy and M. Dormieux for pioneering work on the implementation of the free surface boundary conditions. In addition, all the people involved in the evolution of the FLU3M code are warmly thanked. Finally, the authors wish to thank the Centre National

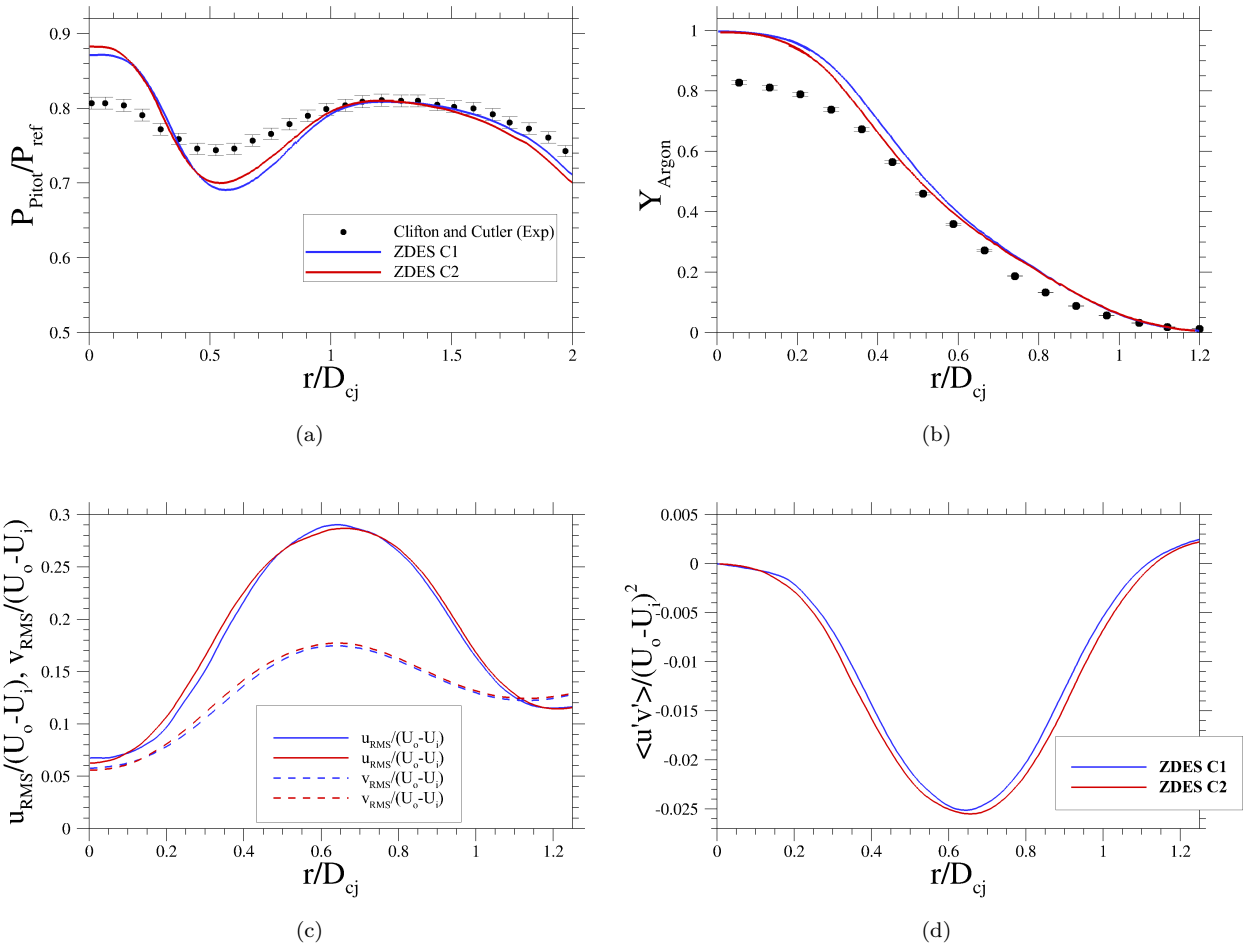

Figure 23: Radial distributions of relative Pitot pressure (a), argon mass fraction (b), rms velocities (c) and total Reynolds shear stress (d) obtained with ZDES at the station X/D_{cj}=26.1.

d'Études Spatiales (CNES) for financial support. The Ph.D. work of J. Reynaud is funded by CNES and ONERA.

References

[1] C. W. Clifton, A. D. Cutler, A supersonic argon/air coaxial jet experiment for computational fluid dynamics code validation, NASA/CR-2007-214866.

[2] S. Deck, N. Renard, Towards an enhanced protection of attached boundary layers in hybrid RANS/LES methods, Journal of Computational Physics 400 (2020) 108970. doi:10.1016/j.jcp.2019.108970.

[3] M. Gusman, J. Housman, C. Kiris, Best practices for CFD simulations of launch vehicle ascent with plumes-overflow perspective, in: 49th AIAA Aerospace Sciences Meeting including the New Horizons Forum and Aerospace Exposition, 2011, p. 1054.

[4] A. Mahjub, N. M. Mazlan, M. Z. Abdullah, Q. Azam, Design optimization of solid rocket propulsion: A

survey of recent advancements, Journal of Spacecraft and Rockets 57 (1) (2020) 3–11. doi:10.2514/1.a34594.

[5] M. Mehta, F. Canabal, S. B. Tashakkor, S. D. Smith, Base heating sensitivity study for a 4-cluster rocket motor configuration in supersonic freestream, Journal of Spacecraft and Rockets Vol. 50, No. 3, May–June 2013.

[6] S. Stephan, J. Wu, R. Radespiel, Propulsive jet influence on generic launcher base flow, CEAS Space Journal 7 (4) (2015) 453–473.

[7] J. P. Drummond, Methods for prediction of high-speed reacting flows in aerospace propulsion, AIAA Journal 52 (3) (2014) 465–485. doi:10.2514/1.j052283.

[8] I. A. Zilberter, J. R. Edwards, Large-Eddy Simulation/Reynolds-averaged Navier–Stokes Simulations of High-Speed Mixing Processes, AIAA Journal 52 (7) (2014) 1486–1501. doi:10.2514/1.j052745.

[9] K. Brinckman, S. Dash, Improved methodology for RANS modeling of high-speed turbulent scalar mixing, in: 50th AIAA Aerospace Sciences Meeting including the New Horizons Forum and Aerospace Exposition, American Institute of Aeronautics and Astronautics, 2012. doi:10.2514/6.2012-567.

[10] P. J. M. Ferrer, R. Buttay, G. Lehnasch, A. Mura, A detailed verification procedure for compressible reactive multicomponent Navier–Stokes solvers, Computers & Fluids 89 (2014) 88–110. doi:10.1016/j.compfluid.2013.10.014.

[11] P. Sagaut, M. Terracol, S. Deck, Multiscale and multiresolution approaches in turbulence-LES, DES and Hybrid RANS/LES Methods : Applications and Guidelines., World Scientific, 2013.

[12] G. Albouze, Simulation aux grandes échelles des écoulements réactifs non prémélangés, Ph.D. thesis, Institut National Polytechnique de Toulouse (2009).

[13] B. Sainte-Rose, Simulations numériques d'écoulements réactifs massivement décollés par une approche hybride RANS/LES, Ph.D. thesis, Châtenay-Malabry, Ecole centrale de Paris (2010).

[14] F. Kozusko, C. Grosch, T. Jackson, C. A. Kennedy, T. Gatski, The structure of variable property, compressible mixing layers in binary gas mixtures, Physics of Fluids 8. doi:10.1063/1.869103.

[15] D. Davidenko, I. Gökalp, E. Dufour, P. Magre, Numerical modeling of inert and reacting compressible turbulent jets, in: AIAA/CIRA 13th International Space Planes and Hypersonics Systems and Technologies Conference, 2005, p. 3237.

[16] J. Reynaud, P. Weiss, S. Deck, Towards binary gas mixture ZDES for space launcher base flow prediction, in: 55 th 3AF International Conference on Applied Aerodynamics Poitiers – France, 2020+1.

[17] R. A. Baurle, J. R. Edwards, Hybrid Reynolds-averaged/large-eddy simulations of a coaxial supersonic freejet experiment, AIAA Journal 48 (3) (2010) 551–571. doi:10.2514/1.43771.

[18] M. Dharavath, P. Manna, D. Chakraborty, Numerical exploration of dissimilar supersonic coaxial jets mixing, Acta Astronautica 111 (2015) 308–316. doi:10.1016/j.actaastro.2015.03.001.

[19] A. Troshin, A. Shiryaeva, V. Vlasenko, V. Sabelnikov, Large-eddy simulation of helium and argon supersonic jets in supersonic air co-flow, in: Progress in Turbulence VIII. iTi 2018. Springer Proceedings in Physics, Vol. 226, Springer International Publishing, 2019, pp. 253–258. doi:10.1007/978-3-030-22196-6_40.

[20] J. Hoste, S. Fechter, S. Karl, K. Hannemann, Study of a supersonic reacting wall jet with a variable turbulent Prandtl and Schmidt number approach, Aerospace Science and Technology 106 (2020) 106070. doi:10.1016/j.ast.2020.106070.

[21] P. Cocks, W. Dawes, R. Cant, DDES of a supersonic coaxial helium jet, in: 50th AIAA Aerospace Sciences Meeting including the New Horizons Forum and Aerospace Exposition, American Institute of Aeronautics and Astronautics, 2012. doi:10.2514/6.2012-479.

[22] S. Deck, Recent improvements in the Zonal Detached Eddy Simulation (ZDES) formulation, Theoretical and Computational Fluid Dynamics 26 (6) (2011) 523–550. doi:10.1007/s00162-011-0240-z.

[23] L. Charrier, G. Pont, S. Marié, P. Brenner, F. Grasso, Hybrid RANS/LES simulation of a supersonic coaxial he/air jet experiment at various turbulent lewis numbers, in: Symposium on Hybrid RANS-LES Methods, Springer, 2016, pp. 337–346.

[24] F. Simon, S. Deck, P. Guillen, P. Sagaut, Reynolds-Averaged Navier-Stokes/Large-Eddy Simulations of supersonic base flow, AIAA Journal 44 (11) (2006) 2578–2590. doi:10.2514/1.21366.

[25] A. Roshko, Structure of turbulent shear flows: a new look, AIAA journal 14 (10) (1976) 1349–1357.

[26] C. Bogey, N. de Cacqueray, C. Bailly, A shock-capturing methodology based on adaptative spatial filtering for high-order non-linear computations, Journal of Computational Physics 228 (5) (2009) 1447–1465. doi:10.1016/j.jcp.2008.10.042.

[27] A. D. Cutler, G. S. Diskin, J. P. Drummond, J. A. White, Supersonic coaxial jet experiment for computational fluid dynamics code validation, AIAA journal 44 (3) (2006) 585–592.

[28] J. Reynaud, P.-E. Weiss, S. Deck, Numerical workflow for scale-resolving computations of space launcher afterbody flows with and without jets, Computers & Fluids 226 (2021) 104994.

[29] F. Ducros, V. Ferrand, F. Nicoud, C. Weber, D. Darracq, C. Gacherieu, T. Poinsot, Large-eddy simulation of the shock/turbulence interaction, Journal of Computational Physics 152 (2) (1999) 517–549. doi:10.1006/jcph.1999.6238.

[30] M.-S. Liou, A sequel to AUSM: AUSM+, Journal of Computational Physics 129 (2) (1996) 364–382. doi:10.1006/jcph.1996.0256.

[31] I. Mary, P. Sagaut, Large Eddy Simulation of Flow Around an Airfoil Near Stall, AIAA Journal 40 (6) (2002) 1139–1145. doi:10.2514/2.1763.

[32] M. Dormieux, P. Guillen, R. Abgrall, Numerical simulation of transverse jet flows by a nonreactive two species multidomain euler flow solver, in: 28th Aerospace Sciences Meeting, 1990, p. 126.

[33] R. Abgrall, Généralisation du schéma de Roe pour le calcul d'écoulement de mélanges de gaz à concentrations variables, La recherche aérospatiale (6) (1988) 31–43.

[34] J. O. Hirschfelder, C. F. Curtiss, R. B. Bird, M. G. Mayer, Molecular theory of gases and liquids, Vol. 165, Wiley New York, 1964.

[35] T. Poinsot, D. Veynante, Theoretical and Numerical Combustion, R.T. Edwards Inc., 2005. URL https://hal.archives-ouvertes.fr/hal-00270731

[36] F. A. Williams, Combustion theory, CRC Press, 2018.

[37] A. Faghri, Y. Zhang, J. R. Howell, Advanced heat and mass transfer, Global Digital Press, 2010.

[38] I. Martinez, Mass diffusivity data, Thermal Data. Departamento de motopropulsão e termo-fluidodinâmica da Universidade Politécnica de Madrid.

[39] S. Deck, Zonal-Detached-Eddy Simulation of the flow around a high-lift configuration, AIAA Journal 43 (11) (2005) 2372–2384. doi:10.2514/1.16810.

[40] P. Spalart, S. Allmaras, A one-equation turbulence model for aerodynamic flows, in: 30th Aerospace Sciences Meeting and Exhibit, American Institute of Aeronautics and Astronautics, 1992. doi:10.2514/6.1992-439.

[41] S. Deck, R. Laraufie, Numerical investigation of the flow dynamics past a three-element aerofoil, Journal of Fluid Mechanics 732 (2013) 401–444. doi:10.1017/jfm.2013.363.

[42] S. Deck, N. Renard, R. Laraufie, P. Sagaut, Zonal Detached Eddy Simulation (ZDES) of a spatially developing flat plate turbulent boundary layer over the Reynolds number range 3 150 $\leq Re_\theta \leq$ 14 000, Physics of Fluids 26 (2) (2014) 025116.

[43] N. Renard, S. Deck, Improvements in zonal detached eddy simulation for wall modeled large eddy simulation, AIAA Journal 53 (11) (2015) 3499–3504.

[44] J. Vaquero, N. Renard, S. Deck, Advanced simulations of turbulent boundary layers under pressure-gradient conditions, Physics of Fluids 31 (11) (2019) 115111.

[45] P. Guillen, M. Dormieux, Design of a 3D multidomain Euler code, in: Supercomputing in fluid flow, 1993, pp. 21–39.

[46] R. Laraufie, S. Deck, P. Sagaut, A dynamic forcing method for unsteady turbulent inflow conditions, Journal of Computational Physics 230 (23) (2011) 8647–8663.

[47] L. Larchevêque, P. Sagaut, T.-H. Lê, P. Comte, Large-eddy simulation of a compressible flow in a three-dimensional open cavity at high Reynolds number, Journal of Fluid Mechanics 516 (2004) 265.

[48] C. Laurent, I. Mary, V. Gleize, A. Lerat, D. Arnal, DNS database of a transitional separation bubble on a flat plate and application to RANS modeling validation, Computers & Fluids 61 (2012) 21–30.

[49] S. Deck, N. Renard, R. Laraufie, P.-É. Weiss, Large-scale contribution to mean wall shear stress in high-Reynolds-number flat-plate boundary layers up to 13650, Journal of Fluid Mechanics 743 (2014) 202–248. doi:10.1017/jfm.2013.629.

[50] N. Renard, S. Deck, On the scale-dependent turbulent convection velocity in a spatially developing flat plate turbulent boundary layer at Reynolds number 13000, Journal of Fluid Mechanics 775 (2015) 105.

[51] P.-É. Weiss, S. Deck, On the coupling of a zonal body-fitted/immersed boundary method with ZDES: Application to the interactions on a realistic space launcher afterbody flow, Computers & Fluids 176 (2018) 338–352. doi:10.1016/j.compfluid.2017.06.015.

[52] P. K. Sweby, High resolution schemes using flux limiters for hyperbolic conservation laws, SIAM journal on numerical analysis 21 (5) (1984) 995–1011.

[53] R. Collercandy, An improved approach for the computation of transonic/supersonic flows with applications to aerospace configurations, in: 10th Applied Aerodynamics Conference, American Institute of Aeronautics and Astronautics, 1992. doi:10.2514/6.1992-2613.
URL https://doi.org/10.2514/6.1992-2613

[54] L. Manueco, P.-E. Weiss, S. Deck, On the coupling of wall-model immersed boundary conditions and curvilinear body-fitted grids for the simulation of complex geometries, Computers & Fluids (2021) 104996.

[55] M. Pechier, Prévisions numériques de l'effet Magnus pour des configurations de munitions, Ph.D. thesis, Poitiers (1999).

[56] T. Coakley, Implicit upwind methods for the compressible Navier-Stokes equations, AIAA journal 23 (3) (1985) 374–380.

[57] M. Pechier, P. Guillen, R. Cayzac, Magnus effect over finned projectiles, Journal of Spacecraft and Rockets 38 (4) (2001) 542–549.

[58] S. Deck, P. Duveau, P. d'Espiney, P. Guillen, Development and application of Spalart–Allmaras one equation turbulence model to three-dimensional supersonic complex configurations, Aerospace Science and Technology 6 (3) (2002) 171–183.

[59] S. Deck, Simulation numérique des charges latérales instationnaires sur des configurations de lanceur, Ph.D. thesis, Orléans (2002).

[60] S. Deck, P.-E. Weiss, N. Renard, A rapid and low noise switch from RANS to WMLES on curvilinear grids with compressible flow solvers, Journal of Computational Physics 363 (2018) 231–255.

[61] A. Spille-Kohoff, H.-J. Kaltenbach, Generation of turbulent inflow data with a prescribed shear-stress profile, Tech. rep., Technische Univ Berlin Germany) Hermann-Fottinger inst fur stromungsmechanik (2001).

[62] J. Vaquero, N. Renard, S. Deck, Advanced simulations of turbulent boundary layers under pressure-gradient conditions, Physics of Fluids 31 (11) (2019) 115111. doi:10.1063/1.5126932.
URL https://doi.org/10.1063/1.5126932

[63] S. Deck, P.-É. Weiss, M. Pamiès, E. Garnier, Zonal detached eddy simulation of a spatially developing flat plate turbulent boundary layer, Computers & Fluids 48 (1) (2011) 1–15. doi:10.1016/j.compfluid.2011.03.009.

[64] F. Simon, Simulations numériques hybrides RANS/LES de l'aérodynamique des projectiles et application au contrôle des écoulements, Ph.D. thesis, Lille 1 (2007).

[65] N.-W. Han, J. Bhakta, R. Carbonell, Longitudinal and lateral dispersion in packed beds: Effect of column length and particle size distribution, AIChE Journal 31 (2) (1985) 277–288.

[66] . Engineering ToolBox (Ed.), Air - Diffusion Coefficients of Gases in Excess of Air.

[67] F. M. White, I. Corfield, Viscous fluid flow, Vol. 3, McGraw-Hill New York, 2006.

[68] E. W. Lemmon, M. O. McLinden, D. G. Friend, Nist chemistry webbook, thermophysical properties of fluid systems, nist standard reference database number 69 (2008).

[69] J. C. R. Hunt, A. A. Wray, P. Moin, Eddies, streams, and convergence zones in turbulent flows, in: Proceedings of the Summer Program, Center for Turbulence Research, Stanford University, 1988, pp. 193–208.

[70] A. Yule, Large-scale structure in the mixing layer of a round jet, Journal of Fluid Mechanics 89 (3) (1978) 413–432.

[71] C. Ball, H. Fellouah, A. Pollard, The flow field in turbulent round free jets, Progress in Aerospace Sciences 50 (2012) 1–26. doi:10.1016/j.paerosci.2011.10.002.

[72] F. Simon, S. Deck, P. Guillen, P. Sagaut, A. Merlen, Numerical simulation of the compressible mixing layer past an axisymmetric trailing edge, Journal of Fluid Mechanics 591 (2007) 215–253.

[73] J. B. Freund, S. K. Lele, P. Moin, Compressibility effects in a turbulent annular mixing layer. part 1. turbulence and growth rate, Journal of Fluid Mechanics 421 (2000) 229–267.

[74] M. Drela, Fluids, Lecture Notes 16, MIT, 2008.

[75] A. Segalini, A. Talamelli, Experimental analysis of dominant instabilities in coaxial jets, Physics of Fluids 23 (2) (2011) 024103. doi:10.1063/1.3553280.

[76] S. Laizet, S. Lardeau, E. Lamballais, Direct numerical simulation of a mixing layer downstream a thick splitter plate, Physics of Fluids 22 (1) (2010) 015104.

[77] R. Mehta, Effect of velocity ratio on plane mixing layer development: Influence of the splitter plate wake, Experiments in fluids 10 (4) (1991) 194–204.

[78] M. M. Ribeiro, J. H. Whitelaw, Turbulent mixing of coaxial jets with particular reference to the near-exit region, Journal of Fluids Engineering 98 (2) (1976) 284–291. doi:10.1115/1.3448288.
URL https://doi.org/10.1115/1.3448288

[79] G. Buresti, P. Petagna, A. Talamelli, Experimental investigation on the turbulent near-field of coaxial jets, Experimental Thermal and Fluid Science 17 (1-2) (1998) 18–26.

[80] D. A. Yoder, J. R. DeBonis, N. J. Georgiadis, Modeling of turbulent free shear flows, Computers & fluids 117 (2015) 212–232.

[81] J. Tan, D. Zhang, H. Li, J. Hou, Detailed experimental investigations on flow behaviors and velocity field properties of a supersonic mixing layer, Acta Astronautica 144 (2018) 30–38.

[82] S. G. Goebel, J. C. Dutton, Experimental study of compressible turbulent mixing layers, AIAA journal 29 (4) (1991) 538–546.

[83] G. L. Brown, A. Roshko, On density effects and large structure in turbulent mixing layers, Journal of Fluid Mechanics 64 (4) (1974) 775–816.

Appendix A. Implicit convective fluxes

The Jacobian matrix of convective fluxes writes as:

$$\begin{pmatrix}
Y_2\mathbf{V}.\mathbf{n} & -Y_1\mathbf{V}.\mathbf{n} & Y_1 n_x & Y_1 n_y & Y_1 n_z & 0 \\
-Y_2\mathbf{V}.\mathbf{n} & Y_1\mathbf{V}.\mathbf{n} & Y_2 n_x & Y_2 n_y & Y_2 n_z & 0 \\
(\rho_2 X + \frac{1}{2}(\gamma-1)\mathbf{V}^2)n_x - u\mathbf{V}.\mathbf{n} & (-\rho_1 X + \frac{1}{2}(\gamma-1)\mathbf{V}^2)n_x - u\mathbf{V}.\mathbf{n} & (2-\gamma)un_x + \mathbf{V}.\mathbf{n} & (1-\gamma)vn_x + un_y & (1-\gamma)wn_x + un_z & (\gamma-1)n_x \\
(\rho_2 X + \frac{1}{2}(\gamma-1)\mathbf{V}^2)n_y - v\mathbf{V}.\mathbf{n} & (-\rho_1 X + \frac{1}{2}(\gamma-1)\mathbf{V}^2)n_y - v\mathbf{V}.\mathbf{n} & (1-\gamma)un_y + vn_x & (2-\gamma)vn_y + \mathbf{V}.\mathbf{n} & (1-\gamma)wn_y + vn_z & (\gamma-1)n_y \\
(\rho_2 X + \frac{1}{2}(\gamma-1)\mathbf{V}^2)n_z - w\mathbf{V}.\mathbf{n} & (-\rho_1 X + \frac{1}{2}(\gamma-1)\mathbf{V}^2)n_z - w\mathbf{V}.\mathbf{n} & (1-\gamma)un_z + wn_x & (1-\gamma)vn_z + wn_y & (2-\gamma)wn_z + \mathbf{V}.\mathbf{n} & (\gamma-1)n_z \\
(\rho_2 X - \gamma e + (\frac{\gamma}{2}-1)\mathbf{V}^2)\mathbf{V}.\mathbf{n} & (-\rho_1 X - \gamma e + (\frac{\gamma}{2}-1)\mathbf{V}^2)\mathbf{V}.\mathbf{n} & (\gamma e + \frac{1}{2}\mathbf{V}^2)n_x - (\gamma-1)u\mathbf{V}.\mathbf{n} & (\gamma e + \frac{1}{2}\mathbf{V}^2)n_y - (\gamma-1)v\mathbf{V}.\mathbf{n} & (\gamma e + \frac{1}{2}\mathbf{V}^2)n_z - (\gamma-1)w\mathbf{V}.\mathbf{n} & \gamma\mathbf{V}.\mathbf{n}
\end{pmatrix} \tag{A.1}$$

Table A.4: Jacobian matrix A of the convective flux with respect to conservative variables (to be multiplied by $\Delta S_{ijk,l}$)

$$J = M^{-1}AM = \begin{pmatrix}
\mathbf{V}.\mathbf{n} & 0 & \rho_1 n_x & \rho_1 n_y & \rho_1 n_z & 0 \\
0 & \mathbf{V}.\mathbf{n} & \rho_2 n_x & \rho_2 n_y & \rho_2 n_z & 0 \\
0 & 0 & \mathbf{V}.\mathbf{n} & 0 & 0 & \frac{n_x}{\rho} \\
0 & 0 & 0 & \mathbf{V}.\mathbf{n} & 0 & \frac{n_y}{\rho} \\
0 & 0 & 0 & 0 & \mathbf{V}.\mathbf{n} & \frac{n_z}{\rho} \\
0 & 0 & \gamma(\gamma-1)\rho e n_x & \gamma(\gamma-1)\rho e n_y & \gamma(\gamma-1)\rho e n_z & \mathbf{V}.\mathbf{n}
\end{pmatrix} \tag{A.2}$$

Table A.5: Jacobian matrix $J = M^{-1}AM$ of the convective flux with respect to primitive variables (to be multiplied by $\Delta S_{ijk,l}$).

Appendix B. Implicit diffusive fluxes

Step 1: Diffusion flux vector G

$$\begin{pmatrix} \rho D^*[\frac{\partial Y_1}{\partial x}n_x + \frac{\partial Y_1}{\partial y}n_y + \frac{\partial Y_1}{\partial w}n_z] \\ \rho D^*[\frac{\partial Y_2}{\partial x}n_x + \frac{\partial Y_2}{\partial y}n_y + \frac{\partial Y_2}{\partial w}n_z] \\ \mu^*[\underbrace{(\frac{4}{3}\frac{\partial u}{\partial x} - \frac{2}{3}\frac{\partial v}{\partial y} - \frac{2}{3}\frac{\partial w}{\partial z})}_{\sigma_{11}}n_x] + \underbrace{(\frac{\partial u}{\partial y} + \frac{\partial v}{\partial x})}_{\sigma_{12}}n_y] + \underbrace{(\frac{\partial u}{\partial z} + \frac{\partial w}{\partial x})}_{\sigma_{13}}n_z] \\ \mu^*[\underbrace{(\frac{\partial u}{\partial z} + \frac{\partial w}{\partial x})}_{\sigma_{31}}n_x + \underbrace{(\frac{\partial w}{\partial y} + \frac{\partial v}{\partial z})}_{\sigma_{32}}n_y + \underbrace{(\frac{4}{3}\frac{\partial w}{\partial z} - \frac{2}{3}\frac{\partial u}{\partial x} - \frac{2}{3}\frac{\partial v}{\partial y})}_{\sigma_{22}}n_y] \\ \mu^*[\underbrace{(\frac{\partial u}{\partial z} + \frac{\partial w}{\partial x})}_{\sigma_{31}}n_x + \underbrace{(\frac{\partial w}{\partial y} + \frac{\partial v}{\partial z})}_{\sigma_{32}}n_y + \underbrace{(\frac{4}{3}\frac{\partial w}{\partial z} - \frac{2}{3}\frac{\partial u}{\partial x} - \frac{2}{3}\frac{\partial v}{\partial y})}_{\sigma_{22}}n_y] \\ G_6 \end{pmatrix} \tag{B.1}$$

With G_6:

$$\begin{aligned} G_6 = [\mu^*(\sigma_{11}u + \sigma_{12}v + \sigma_{13}w) + \lambda^*\frac{\partial T}{\partial x}]n_x + [\mu^*(\sigma_{21}u + \sigma_{22}v + \sigma_{23}w) + \lambda^*\frac{\partial T}{\partial y}]n_y \\ +[\mu^*(\sigma_{31}u + \sigma_{32}v + \sigma_{33}w) + \lambda^*\frac{\partial T}{\partial w}]n_z \\ +D^*(h_1[\frac{\partial Y_1}{\partial x}n_x + \frac{\partial Y_1}{\partial y}n_y + \frac{\partial Y_1}{\partial w}n_z]] + *h_2[\frac{\partial Y_2}{\partial x}n_x + \frac{\partial Y_2}{\partial y}n_y + \frac{\partial Y_2}{\partial w}n_z]) \end{aligned} \tag{B.2}$$

We rewrite some spatial derivatives present in **G** in order to show explicitly the primitive variables:

$$\frac{\partial T}{\partial a} = \frac{\partial \frac{P}{\rho r}}{\partial a} = \frac{\partial P}{\partial a}\frac{1}{\rho r} - \frac{P}{(\rho r)^2}(r_1\frac{\partial \rho_1}{\partial a} + r_2\frac{\partial \rho_2}{\partial a}) \tag{B.3}$$

$$\frac{\partial Y_1}{\partial a} = \frac{\partial \frac{\rho_1}{\rho_2+\rho_1}}{\partial a} = \frac{1}{(\rho_1+\rho_2)^2}(\frac{\partial \rho_1}{\partial a}(\rho_1+\rho_2) - \rho_1(\frac{\partial \rho_1}{\partial a} + \frac{\partial \rho_2}{\partial a})) = \frac{1}{\rho}(Y_2\frac{\partial \rho_1}{\partial a} - Y_1\frac{\partial \rho_2}{\partial a}) \tag{B.4}$$

Step 2: Compute the matrix $(\frac{\partial \boldsymbol{G}}{\partial \boldsymbol{w}_{pa}})_{ijk,l}$ for a = x,y,z

Here as an example, we express the matrix $(\frac{\partial \mathbf{G}}{\partial \mathbf{w}_{px}})_{ijk,l}$ (B.6) for the x coordinate. Similar expressions are found with y and z.

$$\begin{pmatrix} Y_2D^*n_x & -Y_1D^*n_x & 0 & 0 & 0 & 0 \\ -Y_2D^*n_x & Y_1D^*n_x & 0 & 0 & 0 & 0 \\ 0 & 0 & \frac{4}{3}\mu^*n_x & \mu^*n_y & \mu^*n_z & 0 \\ 0 & 0 & -\frac{2}{3}\mu^*n_y & \mu^*n_x & 0 & 0 \\ 0 & 0 & -\frac{2}{3}\mu^*n_z & 0 & \mu^*n_x & 0 \\ (-\lambda^*\frac{T}{\rho}\frac{r_1}{r} + Y_2D^*(h_1-h_2))n_x & (-\lambda^*\frac{T}{\rho}\frac{r_2}{r} + Y_1D^*(h_2-h_1))n_x & \frac{2}{3}\mu^*(2un_x - vn_y - w_nz) & \mu^*(vn_x + un_y) & \mu^*(wn_x + un_z) & \lambda^*\frac{T}{p}n_x \end{pmatrix} \tag{B.5}$$

Table B.6: Partial Jacobian matrix in the x direction $(\frac{\partial \mathbf{G}}{\partial \mathbf{w}_{px}})_{ijk,l}$

Step 3: Compute the Jacobian matrix of G with respect to the primitive variables

We can now add the three matrices derived in the previous step to form: $(\frac{\partial \mathbf{G}}{\partial \mathbf{w}_p})_{ijk,l}$. It is shown in Tab.(B.8).

$$\frac{1}{\Omega}\begin{pmatrix} Y_2 D^* S^2 & -Y_1 D^* S^2 & 0 & 0 & 0 & 0 \\ -Y_2 D^* S^2 & Y_1 D^* S^2 & 0 & 0 & 0 & 0 \\ - & - & \nu^*(\frac{4}{3}S_x^2 + S_y^2 + S_z^2) & 0 & 0 & 0 \\ - & - & - & \nu^*(S_x^2 + \frac{4}{3}S_y^2 + S_z^2) & 0 & 0 \\ - & - & - & - & \nu^*(S_x^2 + S_y^2 + \frac{4}{3}S_z^2) & 0 \\ - & - & - & - & - & (\gamma-1)\lambda^* \frac{T}{p} S^2 \end{pmatrix} \tag{B.6}$$

Table B.7: Jacobian matrix of the viscous flux G with respect to the conservative variables $(\frac{\partial \mathbf{G}}{\partial \mathbf{w}_c})_{ijk,l}$

Step 4: Compute the Jacobian matrix of G with respect to convective variables

We now have to multiply the previously obtained matrix by $M^{-1} = (\frac{\partial \mathbf{w}_p}{\partial \mathbf{w}_c})$ to obtain the Jacobian matrix of the viscous flux $\mathbf{G}$ with respect to the conservative variables $(\frac{\partial \mathbf{G}}{\partial \mathbf{w}_c})_{ijk,l}$. It is shown in Tab.(B.7), only the terms necessary for the computation of eigenvalues are displayed.

Step 5: Use Coakley's method [56] to estimate the contribution of the matrix G

The contribution of the almost triangular matrix obtained in step 4 is evaluated as $(\delta.\frac{S^2}{\Omega})_{ijk,l}.I_6$ with $\delta_{ijk,l} = max(D^*, \frac{4}{3}\nu^*, \frac{\lambda^*}{\rho c_v})_{ijk,l}$.

$$\frac{\mu^*}{\Omega}\begin{pmatrix} Y_2\frac{D^*}{\mu^*}S^2 & -Y_1\frac{D^*}{\mu^*}S^2 & 0 & 0 & 0 & 0 \\ -Y_2\frac{D^*}{\mu^*}S^2 & Y_1\frac{D^*}{\mu^*}S^2 & 0 & 0 & 0 & 0 \\ 0 & 0 & \frac{4}{3}S_x^2+S_y^2+S_z^2 & \frac{1}{3}S_yS_x & \frac{1}{3}S_zS_x & 0 \\ 0 & 0 & \frac{1}{3}S_yS_x & S_x^2+\frac{4}{3}S_y^2+S_z^2 & \frac{1}{3}S_yS_z & 0 \\ 0 & 0 & \frac{1}{3}S_zS_x & \frac{1}{3}S_zS_y & S_x^2+S_y^2+\frac{4}{3}S_z^2 & 0 \\ \frac{S^2}{\mu^*}(-\lambda^*\frac{T}{\rho}\frac{r_1}{r}+Y_2D^*(h_1-h_2)) & \frac{S^2}{\mu^*}(-\lambda^*\frac{T}{\rho}\frac{r_2}{r}+Y_1D^*(h_2-h_1)) & \frac{1}{3}(uS_x^2+vS_xS_y+wS_xS_z)+uS^2 & \frac{1}{3}(uS_xS_y+vS_y^2+wS_yS_z)+vS^2 & \frac{1}{3}(uS_xS_z+vS_zS_y+wS_z^2)+wS^2 & \lambda^*\frac{T}{p\mu*}S^2 \end{pmatrix} \tag{B.7}$$

Table B.8: Jacobian matrix of the viscous flux G with respect to the primitive variables $(\frac{\partial \mathbf{G}}{\partial \mathbf{w}_p})_{ijk,l}$